Independent measurement of extinction and backscatter profiles in cirrus clouds by using a combined Raman elastic-backscatter lidar

Albert Ansmann, Ulla Wandinger, Maren Riebesell, Claus Weitkamp, and Walfried Michaelis

Height profiles of the extinction and the backscatter coefficients in cirrus clouds are determined independently from elastic- and inelastic- (Raman) backscatter signals. An extended error analysis is given. Examples covering the measured range of extinction-to-backscatter ratios (lidar ratios) in ice clouds are presented. Lidar ratios between 5 and 15 sr are usually found. A strong variation between 2 and 20 sr can be observed within one cloud profile. Particle extinction coefficients determined from inelastic-backscatter signals and from elastic-backscatter signals by using the Klett method are compared. The Klett solution of the extinction profile can be highly erroneous if the lidar ratio varies along the measuring range. On the other hand, simple backscatter lidars can provide reliable information about the cloud optical depth and the mean cloud lidar ratio.

Key words: Combined lidar, Raman lidar, backscatter lidar, lidar ratio, particle extinction, particle backscatter, Klett method, cirrus observation.

1. Introduction

High-altitude cirrus clouds have been identified as one important regulator of the radiance balance of the earth-atmosphere system.[1] In particular, optically thin cirrus are of great interest since an increase of the area covered by these clouds, which may be induced partly by contrails, is expected to enhance the greenhouse effect. In spite of the importance of ice clouds, measurements of their microphysical properties (ice-crystal characteristics) and of their radiative properties (extinction, reflection, and emission) are rare[1] mainly because of their high location in the atmosphere. Extended studies of cirrus clouds were performed only recently in two regional experiments, the First International Satellite Cloud Climatology Project (ISCCP) Regional Experiment (FIRE)[2] and the International Cirrus Experiment (ICE).[3] In both investigations high-flying aircraft as well as ground-based observation stations were utilized.

In this paper, lidar measurements taken in cirrus clouds during ICE'89 in September and October 1989 are presented. For what is, to our knowledge, the first time, profiles of the extinction and backscatter coefficients in high-level ice clouds are measured independently of each other with a combined Raman elastic-backscatter lidar. In the technique applied, short laser pulses at a wavelength of 308 nm are transmitted vertically into the atmosphere, and the height profiles of signals elastically backscattered by air molecules and particles (at 308 nm) and inelastically (Raman) backscattered by nitrogen molecules at 332 nm (vibrational-rotational spectrum) are recorded. The particle extinction coefficient is determined from the inelastic-backscatter signal profile,[4] while the particle backscatter coefficient is derived from the ratio of the elastic backscatter to the Raman signal, as is usual in the combined lidar technique.[5,6]

The independent measurement of the particle extinction and backscatter coefficients and, thus, of the extinction-to-backscatter ratio, or lidar ratio, provides information on the transmission and the reflection properties of cirrus clouds and also on the ice-crystal characteristics because the lidar ratio depends on shape, size, and orientation of the anisotropic ice particles. The influence of the microphysical properties on the extinction-to-backscatter ratio is discussed here on the basis of measurement examples.

The lidar ratio is one important input parameter

The authors are with the Institut für Physik, GKSS-Forschungszentrum Geesthacht GmbH, Postfach 1160, W-2054 Geesthacht, Germany.

Received 5 June 1991.
0003-6935/92/337113-19$05.00/0.

for the determination of the particle extinction coefficient from the elastic-backscatter signal alone.[7–10] In this technique, which originates from Hitschfeld and Bordan's radar application,[11] the particle extinction or backscatter coefficient is obtained by solving a Bernoulli equation that is derived from the basic lidar equation with the assumption of a power-law relationship between aerosol extinction and backscattering. The technique is often referred to as the Klett method, as Klett[8] reformulated the formalism in a manner convenient for the analysis of lidar observations. The method is widely used because most lidars are elastic-backscatter lidars. Measurements of the extinction-to-backscatter ratio are, therefore, also valuable for the application of this technique.

Furthermore, the independent measurement of backscatter and extinction profiles offers the opportunity to analyze the validity of the Bernoulli solution. In fact, the determination of the extinction coefficients from the Raman signals is the only way to obtain reliable cirrus extinction profiles. This is shown here by comparing the results of the two techniques under different extinction and backscatter conditions, i.e., for different values of a range-dependent lidar ratio.

In principle, the high spectral resolution lidar (HSRL) technique can also provide accurate extinction data.[12] Here the spectral distribution of the elastically backscattered light is measured, and the narrow aerosol backscatter peak is separated from the Doppler-broadened Rayleigh line. The molecular backscatter profile is then used to determine the particle extinction coefficient. At the present stage,[13] however, the suppression of strong ice-crystal scattering in the Rayleigh measurement channels is not sufficient and the determination of cirrus extinction profiles is not yet possible.

Although the Bernoulli solution of the extinction coefficient is uncertain for cirrus, the formalism can be applied to calculate the mean cloud lidar ratio together with the cloud optical depth. This is demonstrated on the basis of the results of a cirrostratus measurement.

This paper contains six sections. The introduction is followed by a description of the lidar apparatus. In Section 3 the basic equations for the determination of the quantities of interest are given. Section 4 presents an extended error analysis, which is necessary because Raman signals are used for what is, to our knowledge, the first time for comprehensive studies of cloud optical properties. In Section 5 experimental results are shown and discussed. A summary is given in Section 6.

2. Lidar Apparatus

The essential technical data of the combined Raman elastic-backscatter lidar are summarized in Table 1.[14,15] The lidar system is based on a powerful XeCl excimer laser. Afocal optics pointing to the zenith are used at both the transmitting and receiving end of the lidar. The laser beam is expanded tenfold. It enters the receiver field of view (RFOV) at a tilt angle of 0.1 to 0.2 mrad. The entire setup is mounted on one table that can be tilted up to 30 mrad. The RFOV axis is adjusted vertically with a spirit level; the uncertainty is less than 1 mrad.

Table 1. Technical Data of the Combined Raman Elastic-Backscatter Lidar

Laser	
Type	Lambda Physik EMG 203 MSC
Wavelength	308 nm
Pulse energy	270 mJ
Repetition frequency	250 Hz
Resonator	unstable
Divergence	1 mrad
Pulse duration	20 ns
Transmitter optics	
Geometry	Afocal Cassegrain
Main mirror	400 mm, $f/3.75$
Divergence of the expanded laser beam	0.1 mrad
Receiver optics	
Geometry	Afocal Cassegrain
Main mirror	800 mm, $f/3.75$
Field of view	0.2 mrad
Dispersion system	
Type	3-channel filter polychromator
Channel	Elastic backscatter/N_2 Raman
Wavelength	308 nm/332 nm
Bandwidth	2.5 nm/5.0 nm
Transmittance	0.6%/10.4%
Photomultipliers	Thorn EMI 9893 QB 350
Data acquisition system	
Type	3-input-channel multichannel scaler
Model	MEDAV PURANA
Maximum count rate	300 MHz
Minimum time-bin width	100 ns

A 0.8-m-diameter telescope collects backscattered radiation from particles and air molecules. When leaving the telescope the beam is 80 mm in diameter. It is focused onto an entrance diaphragm and recollimated to 8 mm in diameter. The RFOV can be varied by a change of the field stop aperture. A field of view of 0.2 mrad is normally used. This is a compromise that results in a tolerable background level and an acceptable range of complete overlap between laser beam and RFOV from 1.5 km to heights above the tropopause. For measurements at shorter ranges the axes of the laser beam and the RFOV can be made to intersect at some finite height down to ~400 m.

To separate the 308-nm (elastic-backscatter) and 332-nm (nitrogen Raman-backscatter) radiation, a polychromator equipped with interference filters is used.[15] The narrow-bandpass filters select the wavelengths of interest, reduce sky background radiation, and, for the nitrogen Raman channel, block the strong elastic-backscatter radiation at the laser wavelength; the suppression of 308-nm light is better than 10^{-8}.[15] This value is sufficient as the nitrogen Raman signal is 10^3 times smaller than the Rayleigh

backscatter signal, and a particle backscatter signal no more than a factor of 10^3 larger than the Rayleigh backscatter signal can be assumed. Even in the case of strong backscattering from cloud base regions, these conditions are always met at $\lambda = 308$ nm, as our measurements show. The elastic-backscatter channel is attenuated by additional neutral density filters to reduce its count rate below 100 MHz, the maximum value for which dead-time corrections[14,16] of the 300-MHz system remain at a reasonable level.

The photomultiplier tubes are operated in the photon counting mode. The dark current of each photomultiplier is less than 1 count/s. A computer-controlled multichannel scaler registers the pulses at a maximum sampling rate of 10 MHz, which corresponds to a depth resolution of 15 m. The data acquisition electronics are triggered by a photomultiplier tube that senses the outgoing laser pulse. Count rates are corrected for photomultiplier dead time and, in the case of daytime measurements of elastic-backscatter signals, for background noise. For the determination of the mean sky background, data from the height range between 16 and 18 km were taken. At nighttime, the background level was negligibly small for both measurement channels.

During the field campaign of ICE'89 backscatter signals were accumulated in 60-m height intervals up to an altitude of 18 km and in time intervals of 1 min or more. The location of the combined Raman elastic-backscatter lidar was on the North Sea island of Norderney (longitude 7°13'E, latitude 53°43'N). The lidar was part of a mesoscale network made up of four ground-based lidar stations arranged in and around the German Bight.[17] Accompanying radiosonde ascents were also made at Norderney to yield the actual temperature and pressure profiles.

As mentioned above, vertical pointing of the receiver optics was selected during ICE'89. This does not appear to be the best choice for studies of cirrus scattering and extinction properties if specular reflection by horizontally oriented ice crystals occurs. Details on that problem are given in Sections 4 and 5. The measurement conditions were determined by the fact that a polarization lidar, taking measurements of the depolarization ratio on a routine basis, was a member of the net. It is believed that the most interesting results are obtained if this lidar looks vertically. Thus, all four lidars were pointed to the zenith in order to make the results of the network comparable. Furthermore, we believe that the entire range of cirrus extinction-to-backscatter ratios can be observed only under these conditions.

3. Theory

The measurement of the elastic-backscatter signal at 308 nm and of the nitrogen inelastic-backscatter signal at 332 nm permits the determination of the extinction and backscatter coefficients independently of each other and, thus, of the extinction-to-backscatter ratio.

The basic lidar equation for the elastic-backscatter signal is

$$P_{\lambda_0}(z) = K_{\lambda_0}\frac{O(z)}{z^2}\left[\beta_{\lambda_0}{}^{\mathrm{aer}}(z) + \beta_{\lambda_0}{}^{\mathrm{mol}}(z)\right] \times \exp\left\{-2\int_0^z \left[\alpha_{\lambda_0}{}^{\mathrm{aer}}(\zeta) + \alpha_{\lambda_0}{}^{\mathrm{mol}}(\zeta)\right]\mathrm{d}\zeta\right\}, \quad (1)$$

and for the nitrogen Raman-backscatter signal is

$$P_{\lambda_R}(z) = K_{\lambda_R}\frac{O(z)}{z^2}N_R(z)\frac{\mathrm{d}\sigma_{\lambda_R}(\pi)}{\mathrm{d}\Omega} \times \exp\left\{-\int_0^z \left[\alpha_{\lambda_0}{}^{\mathrm{mol}}(\zeta) + \alpha_{\lambda_0}{}^{\mathrm{aer}}(\zeta) + \alpha_{\lambda_R}{}^{\mathrm{mol}}(\zeta) + \alpha_{\lambda_R}{}^{\mathrm{aer}}(\zeta)\right]\mathrm{d}\zeta\right\}. \quad (2)$$

Here P_{λ_0} and P_{λ_R} are the powers received from distance z at the laser wavelength λ_0 and at the Raman wavelength λ_R, respectively. $O(z)$ is the laser beam RFOV overlap function, which is unity for heights greater than the minimum measurement height $z_{\min}$ above which the laser beam completely overlaps with the field of view of the receiver. K_{λ_0} and K_{λ_R} contain all depth-independent system parameters. $N_R(z)$ is the nitrogen molecule number density, $\mathrm{d}\sigma_{\lambda_R}(\pi)/\mathrm{d}\Omega$ is the range-independent differential Raman cross section for the backward direction, and $\beta_{\lambda_0}{}^{\mathrm{mol}}$ and $\beta_{\lambda_0}{}^{\mathrm{aer}}$ are the backscatter coefficients that are due to Rayleigh and particle scattering. The coefficients $\alpha_{\lambda_0,\lambda_R}{}^{\mathrm{mol}}$ and $\alpha_{\lambda_0,\lambda_R}{}^{\mathrm{aer}}$ describe the extinction that is due to absorption and Rayleigh scattering by atmospheric gases and aerosol extinction for the laser and the Raman wavelengths λ_0 and λ_R, respectively.

Several attempts have been made to derive the particle extinction coefficient or the aerosol transmission directly from the measured Raman signal profile of a gas of known density (e.g., oxygen or nitrogen).[4,18–21] As was shown previously,[4] the particle extinction coefficient can be obtained from the nitrogen Raman signal by means of Eq. (2) by the use of

$$\alpha_{\lambda_0}{}^{\mathrm{aer}}(z) = \frac{\dfrac{\mathrm{d}}{\mathrm{d}z}\left[\ln\dfrac{N_R(z)}{P_{\lambda_R}(z)z^2}\right] - \alpha_{\lambda_0}{}^{\mathrm{mol}}(z) - \alpha_{\lambda_R}{}^{\mathrm{mol}}(z)}{1 + \left(\dfrac{\lambda_0}{\lambda_R}\right)^k}, \quad (3)$$

where particle scattering is assumed to be proportional to λ^{-k}. For aerosol particles and water droplets with diameters comparable with the measurement wavelength, $k = 1$ is appropriate, while in the case of ice particles, which are usually large compared with the laser wavelength, $k = 0$ is justified.[22] The air density and the Rayleigh scattering and ozone absorption coefficients must be known for the determination of $N_R(z)$ and $\alpha_{\lambda_0,\lambda_R}{}^{\mathrm{mol}}(z)$ in Eq. (3). Air density and the Rayleigh scattering coefficient are determined from actual radiosonde data of tempera-

ture and pressure, if available, or from a standard atmosphere model fitted to measured ground-level temperature and pressure values. The ozone absorption coefficient is estimated from measured absorption cross sections[23] and the ozone density model for midlatitude summer conditions.[24]

The particle backscatter coefficient $\beta_{\lambda_0}^{aer}(z)$ can be determined by using both elastically and inelastically backscattered signals.[5,6] Two measured signal pairs P_{λ_0} and P_{λ_R} at height z and at a reference height z_0 are needed. From two lidar equations [see Eq. (1)] for the elastic-backscatter signals $P_{\lambda_0}(z)$ and $P_{\lambda_0}(z_0)$ and two Raman lidar equations [see Eq. (2)] for $P_{\lambda_R}(z)$ and $P_{\lambda_R}(z_0)$, a solution for the particle backscatter coefficient $\beta_{\lambda_0}^{aer}(z)$ is obtained by forming the ratio

$$\frac{P_{\lambda_0}(z)P_{\lambda_R}(z_0)}{P_{\lambda_0}(z_0)P_{\lambda_R}(z)},$$

inserting the respective lidar equations for the four signals, and rearranging the resulting equation. The solution is

$$\beta_{\lambda_0}^{aer}(z) = -\beta_{\lambda_0}^{mol}(z) + [\beta_{\lambda_0}^{aer}(z_0) + \beta_{\lambda_0}^{mol}(z_0)] \times \frac{P_{\lambda_R}(z_0)P_{\lambda_0}(z)N_R(z)}{P_{\lambda_0}(z_0)P_{\lambda_R}(z)N_R(z_0)} \times \frac{\exp\left\{-\int_{z_0}^{z}[\alpha_{\lambda_R}^{aer}(\zeta) + \alpha_{\lambda_R}^{mol}(\zeta)]d\zeta\right\}}{\exp\left\{-\int_{z_0}^{z}[\alpha_{\lambda_0}^{aer}(\zeta) + \alpha_{\lambda_0}^{mol}(\zeta)]d\zeta\right\}}. \quad (4)$$

The reference height z_0 is usually chosen such that $\beta_{\lambda_0}^{mol}(z_0) \gg \beta_{\lambda_0}^{aer}(z_0)$, so that $\beta_{\lambda_0}^{aer}(z_0) + \beta_{\lambda_0}^{mol}(z_0) \simeq \beta_{\lambda_0}^{mol}(z_0)$. These clear air conditions normally prevail in the upper troposphere. At high altitudes the background level of the particle-to-Rayleigh-backscatter ratio is less than 0.01 for $\lambda = 308$ nm at midlatitudes.[25] Then only the air density, the molecular backscattering, and atmospheric extinction properties must be estimated to solve Eq. (4). This can be done as described above. The particle transmission ratio for the height range between z_0 and z is determined from the measured particle extinction coefficients [see Eq. (3)] with the assumption of a wavelength dependence of λ^{-1} below clouds and in water clouds and no wavelength dependence in cirrus.

In the case of a high particle load throughout the whole troposphere, a situation that did not occur during ICE'89, a value of $\beta_{\lambda_0}^{aer}(z_0)$ in Eq. (4) is needed. This quantity cannot be estimated with sufficient accuracy from the determined particle extinction coefficient, because the particle extinction-to-backscatter ratio $S_{\lambda_0}^{aer}(z_0) = \alpha_{\lambda_0}^{aer}(z_0)/\beta_{\lambda_0}^{aer}(z_0)$ is not known well enough, even if published data of this parameter for different aerosol types[26] are used. In this special case a determination of the backscatter profile from Eq. (4) is not possible. However, such a situation seldom occurs. Even after the strong eruptions of Mt. Pinatubo in June 1991, which resulted in enhanced stratospheric aerosol content and sinking particles penetrating through the tropopause, the upper troposphere above 5 km was usually clean, as our measurements show.

Finally, the height profile of the lidar ratio,

$$S_{\lambda_0}^{aer}(z) = \frac{\alpha_{\lambda_0}^{aer}(z)}{\beta_{\lambda_0}^{aer}(z)}, \quad (5)$$

can be obtained from the profiles of $\alpha_{\lambda_0}^{aer}(z)$ and $\beta_{\lambda_0}^{aer}(z)$, as determined with Eqs. (3) and (4).

With the present experimental setup Raman lidar applications are limited to nighttime because the weak inelastic-backscatter signal can be detected only in the absence of the strong daylight background. For daytime observations of cirrus clouds only the elastic-backscatter signal can be used. For this reason the analysis of the applicability of the inversion method[7–10] for the determination of cirrus scattering properties is presented in the sections below. The solution of the Bernoulli equation in terms of the particle extinction coefficient can be written as[10]

$$\alpha_{\lambda_0}^{aer}(z) + \frac{S_{\lambda_0}^{aer}(z)}{S_{\lambda_0}^{mol}}\alpha_{\lambda_0}^{mol}(z) = \frac{S_{\lambda_0}^{aer}(z)P_{\lambda_0}(z)z^2 \exp\left\{-2\int_{z_0}^{z}\left[\frac{S_{\lambda_0}^{aer}(\zeta)}{S_{\lambda_0}^{mol}} - 1\right]\alpha_{\lambda_0}^{mol}(\zeta)d\zeta\right\}}{\frac{S_{\lambda_0}^{aer}(z_0)P_{\lambda_0}(z_0)z_0^2}{\alpha_{\lambda_0}^{aer}(z_0) + \frac{S_{\lambda_0}^{aer}(z_0)}{S_{\lambda_0}^{mol}}\alpha_{\lambda_0}^{mol}(z_0)} - 2\int_{z_0}^{z} S_{\lambda_0}^{aer}(\zeta)P_{\lambda_0}(\zeta)\zeta^2 \exp\left\{-2\int_{z_0}^{\zeta}\left[\frac{S_{\lambda_0}^{aer}(\xi)}{S_{\lambda_0}^{mol}} - 1\right]\alpha_{\lambda_0}^{mol}(\xi)d\xi\right\}d\zeta}. \quad (6)$$

$S_{\lambda_0}^{mol} = (8\pi/3)$ sr and $S_{\lambda_0}^{aer}(z)$ are the extinction-to-backscatter ratios for Rayleigh and particle scattering, respectively. The lidar ratio $S_{\lambda_0}^{aer}(z)$ must be estimated and, for favorable conditions, can be taken from the literature.[26] z_0 is the reference or calibra-

tion height for which the particle extinction coefficient $\alpha_{\lambda_0}^{aer}(z_0)$, i.e., the boundary value of the integration, must be estimated in addition to the particle lidar ratio $S_{\lambda_0}^{aer}(z)$. Equation (6) can, in principle, be integrated by starting from the calibration height z_0, which may be either the near end ($z > z_0$, forward integration) or the remote end of the measuring range ($z < z_0$, backward integration). Numerical stability, which is not to be mistaken for accuracy, is, however, given only in the backward integration case.[8] Equation (6) assumes only particle and Rayleigh scattering. Absorption by ozone, which is not negligible at $\lambda_0 = 308$ nm, must be corrected before the Klett method is applied. Rayleigh scattering and ozone absorption coefficients are determined in the way described above by use of standard model assumptions or measured data.

The particle backscatter coefficient is then obtained from Eq. (6) by dividing the resultant extinction coefficient $\alpha_{\lambda_0}^{aer}(z)$ by the lidar ratio $S_{\lambda_0}^{aer}(z)$, which was used before to solve Eq. (6).

4. Error Analysis

Three sources of uncertainties determine the error of the parameters calculated with Eqs. (3)–(6): the statistical error caused by signal or photon noise, a systematic error that results from uncertainties in the input parameters, and an error introduced by operational procedures such as signal averaging during varying atmospheric extinction and scattering conditions. In this section the treatment of real (noisy) lidar signals is described, and the errors of the obtained solutions are discussed. The statistical error is estimated by applying the law of error propagation and Poisson statistics, i.e., by assuming that the standard error (noise) of the total number of photon events (signal) is equal to the square root of the total number of events. In the figures below, standard deviations are indicated by error bars. The systematic error and the uncertainty that is due to variations of optical properties during signal acquisition are estimated by numerical simulation. The influence of statistical noise and atmospheric backscatter fluctuations on lidar results has already been discussed in some detail.[13,27,28] Nevertheless, we believe that a satisfactory analysis of errors introduced by varying aerosol or cloud optical properties has not been made previously.

A. Particle Extinction Coefficients from the Raman Lidar Method

In Fig. 1 two examples of the measurement of the particle extinction coefficient, determined after Eq. (3), are shown. A cirrus measurement is given in Fig. 1(a). An aerosol extinction profile of the lower troposphere, starting in the middle of the boundary layer, is presented in Fig. 1(b). During ICE'89, extinction coefficients were not determined for the lowest heights.

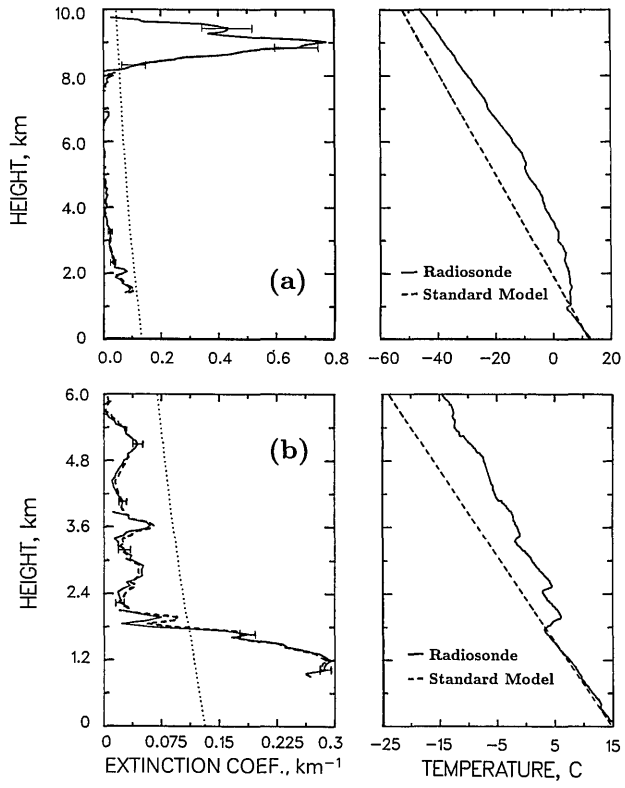

Fig. 1. Particle extinction coefficient measured with a Raman lidar on (a) 24 October 1989 between 1809 and 1821 local time (lt) and on (b) 5 September 1989 between 2153 and 2219 lt. The solid curve of the particle extinction coefficient is calculated by using actual radiosonde data of temperature (right-hand side, solid curve) and pressure. The dashed curve is obtained by assuming standard-atmosphere conditions for temperature (right-hand side, dashed curve) and pressure. The Rayleigh extinction coefficient (dotted curve) is shown for comparison. The discontinuities at 2.4 km and 8.1 km in (a) and at 2.1 km and 3.9 km in (b) reflect the change of the gliding average window length Δz in the smoothing of the corrected signal profile and in the calculation with Eq. (7) from 180 to 600 m and back to 300 m and from 120 to 300 m and 600 m, respectively. The apparent resolution results from a gliding calculation step width of 60 m.

For each profile a large number of laser shots is averaged. Even so, the resulting lidar signal profile must be smoothed in order to reduce the relative statistical error to a tolerable level of 10–20%. 90,695 and 244,528 laser shots are added up for the profiles of Fig. 1(a) and 1(b), respectively; at the maximum repetition rate of the laser of 250 Hz (see Table 1) these shots are transmitted within 6 and 16 min, respectively. Actual measurement times Δt, however, was 12 and 26 min because corrosion of the laser tube limited the maximum pulse repetition rate during the experiment to ~150 Hz.

Before the signal profile is smoothed, the time-averaged lidar signals $\overline{P_{\lambda_R}}(z, \Delta t)$ are corrected for range and molecular scattering and extinction, so that only the dependence on particle extinction remains [see Eq. (2)]. This makes up for a small fraction of total lidar signal variability. After smooth-

ing the corrected signals $\overline{P_{\lambda_R,C}}(z, \Delta t)$ by forming a sliding average of window length Δz, the particle extinction coefficient is obtained from Eq. (3) as

$$\overline{\alpha_{\lambda_0}^{\text{aer}}}(z, \Delta z, \Delta t) = \frac{1}{\Delta z\left[1 + \left(\frac{\lambda_0}{\lambda_R}\right)^k\right]} \times \ln\left[\frac{\overline{P_{\lambda_R,C}}(z - 0.5\Delta z, \Delta t)}{\overline{P_{\lambda_R,C}}(z + 0.5\Delta z, \Delta t)}\right]. \quad (7)$$

Sources of systematic errors in the particle extinction determination are uncertainties of the estimates of the temperature, pressure, and ozone density profiles, and of the wavelength dependence parameter k.

The influence of an error in the estimate of the temperature profile is shown in Fig. 1. While the solid curves of the particle extinction coefficient are calculated with actual data of temperature and pressure measured with a radiosonde launched at the lidar station, the dashed curves are determined by the use of the following simple assumptions for the profiles of temperature $T(z)$ and pressure $p(z)$:

$$T(z) = T(0) + \frac{dT}{dz} z, \quad (8)$$

$$p(z) = p(0)\exp(-z/z_p), \quad (9)$$

where the temperature gradient $dT/dz = -6.5$ K/km, the pressure scale height $z_p = 7.8$ km, and the ground-level values of temperature and pressure are $T(0)$ and $p(0)$, respectively. Relations (8) and (9) represent approximately standard-atmosphere conditions. The temperature profiles calculated after Eq. (8) are also shown in Fig. 1.

The most significant contribution to $\delta\alpha_{\lambda_0}^{\text{aer}}(z)$ results from an error in the estimated temperature gradient. The error of dT/dz affects the calculation of $d[\ln N_R(z)]/dz$ in Eq. (3), i.e., the correction of the air density decrease with height. As can be seen in Fig. 1(b), a large error $\delta\alpha_{\lambda_0}^{\text{aer}}(z)$, i.e., a considerable deviation of the dashed from the solid curve, occurs at the height of 1.9 km, where a strong temperature inversion with a temperature gradient of +13 K/km is present, causing an error of $\delta\alpha_{\lambda_0}^{\text{aer}}(z) = 0.032$ km^{-1}. The influence of an error of dT/dz decreases with increasing smoothing window length Δz. Therefore two inversion layers with somewhat smaller depths, which occur at 2.5 km and at 3.4 km where the smoothing window length Δz is 300 m, have a much smaller effect.

The influence of temperature uncertainty is small and usually negligible when strong inversion layers are absent [see Fig. 1(a)] so that the error of the temperature gradient estimate is small. Then only the correction of the Rayleigh extinction in Eq. (3) is affected. For example, the combined errors of $\delta T = -10$ K and $\delta p = +1$ kPa cause an error of the particle extinction coefficient of only +0.004 km^{-1}.

An additional contribution to $\delta\alpha_{\lambda_0}^{\text{mol}}$ results from the uncertainty in the estimate of the ozone density. $\delta\alpha_{\lambda_0}^{\text{aer}} \simeq \pm 0.006$ km^{-1} is caused if an ozone density profile according to the midlatitude summer model[24] is assumed, and the (true) ozone content is either negligible or a factor of 2 higher than assumed. In Fig. 1(a), the ozone density may be overestimated. As a consequence, a few particle extinction values between 5 and 8 km in height come out negative [see Eq. (3)].

In Fig. 1, a wavelength dependence parameter $k = 1$ is used except for the cirrus between 8 and 10 km in height, where it is set to $k = 0$. A deviation of the true wavelength dependence parameter in Eqs. (3) or (8) from the estimated k by 0.5 or 1 causes a relative error of $\alpha_{\lambda_0}^{\text{aer}}$ of less than 2% and 4%, respectively.

An additional systematic error that is due to multiple scattering must be generally considered in the interpretation of extinction profiles derived from lidar measurements in clouds. Under conditions of intense scattering, photons scattered out of the incident beam can be partly redirected into the RFOV. As a consequence, the derived extinction coefficient is smaller than the extinction coefficient that would result if only single-scattered light entered the receiver telescope. The multiple-scattering effect can be estimated as a function of RFOV and laser beam divergence, optical depth of the cloud, the distance from the lidar, and scattering characteristics of cloud particles.[29] The influence is found to be small for the lidar system parameters as presented in Table 1. For example, in the case of a 4-km-deep cirrus with a cloud base at 7-km height, with scattering conditions according to a range-independent extinction coefficientof 0.4 km^{-1}, and particle-scattering parameters for a typical cirrus,[30] the effective particle extinction coefficient is estimated to be between 12% and 4% smaller than corresponding single-scattering values for the height regions between 7 and 8 km and 10 and 11 km, respectively. For a cumulus cloud and the respective scattering parameters[31] with a base height at 5 km and a range-independent extinction coefficient of 10 km^{-1}, the deviation of the effective from the single-scattering extinction coefficient is between 10% at the cloud base (between 5.0 and 5.1 km) and less than 3% inside the water cloud.

Because of the necessary signal averaging an additional and significant error can be introduced in the solution of Eq. (7) if the particle optical properties vary strongly during the measurement, even if only a few shots are averaged. After Eq. (7) the mean local extinction coefficient in the range cell Δz for the sampling interval Δt is calculated from the difference of the logarithms of mean transmission values

$$\overline{\exp\left\{-\int_0^z [\alpha_{\lambda_0}^{\text{aer}}(\zeta) + \alpha_{\lambda_R}^{\text{aer}}(\zeta)]d\zeta\right\}},$$

not from the difference of mean optical depths

$$\overline{\int_0^z [\alpha_{\lambda_0}{}^{aer}(\zeta) + \alpha_{\lambda_R}{}^{aer}(\zeta)]d\zeta},$$

which would give the correct solution in all cases of variable particle extinction conditions. From a theoretical point of view, the desired mean extinction coefficient in the range cell Δz is obtained only if the optical properties are constant over the measurement and averaging time period Δt, because only then does the averaging of transmissions, i.e., of Raman signals, and of optical depths lead to the same solution of Eq. (7). In practice, this condition is sufficiently well met if the particle extinction is approximately constant or if the varying total optical depth between the lidar and the measurement height is much smaller than unity during the lidar measurement. These conditions are typical for aerosol layers and thin cirrus clouds. If the optical properties of the atmosphere vary strongly between 0 and >1, the error of $\overline{\alpha_{\lambda_0}{}^{aer}}(z, \Delta z, \Delta t)$ can be large.

This is demonstrated in Fig. 2. The total measurement time Δt is divided into like intervals Δt_1 and Δt_2. A rapid increase of the particle extinction from 0 to ~ 2 km^{-1} (Fig. 2) or more is often observed when broken cumulus or stratus clouds pass the RFOV. The profile of the mean transmission in Fig. 2(b) is used to calculate the extinction coefficient in Fig. 2(c) after Eq. (7). The mean transmission for a sampling period $\Delta t = \Delta t_1 + \Delta t_2$ is obtained by averaging the backscattered nitrogen Raman signals measured during the respective time, dividing the signals by the system parameter $K_{\lambda_R} O(z)$ [see Eq. (2)], and correcting them for the range and molecular extinction and density effects.

As can be seen in Fig. 2(c), the solution $\overline{\alpha_{\lambda_0}{}^{aer}}(z, \Delta z, \Delta t)$ deviates significantly from the mean extinction coefficient in the layer between 600 and 1200 m, where particle extinction increases rapidly. The relative error is large in this height region and small below the cloud layer, where particle extinction does not vary strongly. The error increases with increasing optical depth or decreasing transmission [see Fig. 2(b), solid curve] between the ground and the measurement cell Δz, i.e., with increasing height.

If the total sampling period Δt is divided into 5 instead of 2 sections and the particle extinction increases linearly during Δt, the relative error is between 2 and 1.6 times smaller than the error shown in Fig. 2(d) for the height region between 600 and 1200 m. Thus, for smoothly changing cirrus scattering conditions with cloud optical depth values between 0 and 1, a systematic underestimation of the extinction coefficient of the order of 10% in the cloud base region and of 30% in the upper parts of the cloud has to be taken into account. For thin cirrus with an

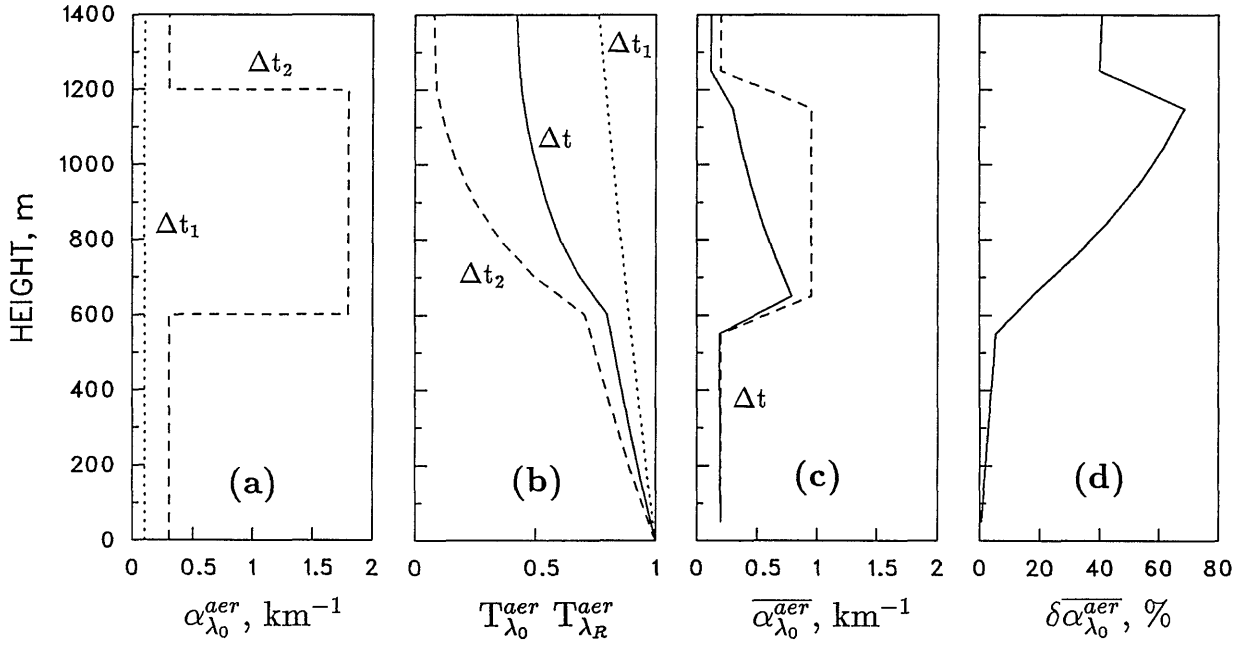

Fig. 2. Modeled error of the extinction coefficient caused by averaging of Raman backscatter signals measured during a time period Δt of strongly varying particle extinction conditions. (a) Simulated particle extinction for the first (dotted line) and second half (dashed curve) of the total sampling period $\Delta t = \Delta t_1 + \Delta t_2$. (b) Particle transmissions calculated from the extinction profiles shown in (a) for the two-way path from the lidar to the backscatter height [see Raman lidar equation (2)]; individual transmissions for Δt_1 (dotted line) and Δt_2 (dashed curve), and averaged transmission profile (solid curve). In a lidar measurement the mean transmission profile is derived from the averaged Raman backscatter signal profile measured during the total sampling interval Δt. (c) Particle extinction coefficient determined from the mean transmission profile for the period Δt after Eq. (7) (solid curve), and the true mean extinction coefficient calculated from the individual transmission profiles for Δt_1 and Δt_2 (dashed curve). Range resolution $\Delta z = 100$ m. (d) Relative error of the derived particle extinction coefficient.

optical depth of 0.2 or less the relative error is below 10%.

The question of whether the smoothing of signals that can lead to considerable errors in optically thick clouds introduces any additional error was also investigated for the present case. It turned out that in all practical events of the ICE'89 campaign no additional error from sliding data averaging occurred.

Errors of the kind shown in Fig. 2 can be reduced or avoided by dividing the total measurement time period into intervals with constant particle extinction conditions. The mean extinction coefficient is then obtained by calculating the extinction profile for each time interval and by averaging the resulting extinction profiles. For an appropriate division of the total time into intervals signal profiles must be stored with high resolution. Time sections of nearly constant particle extinction can then be determined from the time series of the elastic-backscatter profiles. But, in general, and this is what we wanted to demonstrate with Fig. 2, one must be careful in the interpretation of measurement results if particle optical properties vary strongly, e.g., in inhomogeneous and variable fields of thick cirrus and water clouds.

Averaging the logarithms of the signals, although theoretically leading to the correct solution, is, in practice, not preferable because of the low signal-to-noise ratio of the raw lidar data profiles and the new systematic errors introduced by averaging the logarithms of noisy data.[28]

A sufficiently small optical depth throughout the entire measurement region is always given in cloud-free regions, as is the case in Fig. 1(a) below 8 km in height, in Fig. 1(b), and in optically thin cirrus clouds. In Fig. 1(a), an optically thick cirrus is shown. The error, however, is believed to be small because the cloud optical depth, which is determined from the high-resolution Raman signal profiles for successive two-minute intervals, varies smoothly between 0.5 and 1. For such a case, the simulation performed as described above (Fig. 2) shows that the extinction coefficient in the cloud is underestimated by ~10%.

So great care must be taken in the averaging of the lidar signals if the particle scattering properties vary strongly. The error of the particle-extinction coefficient that is due to this effect can be larger than 20% in typical cirrus clouds. The most important atmospheric input parameter is the temperature gradient. A significant error can occur if a temperature inversion is present and standard atmospheric conditions are assumed. In practice, because of the combined effect of the uncertainties in the estimated ozone density, in temperature and pressure profiles, and in the temperature gradient, an error $\delta\alpha_{\lambda_0}^{aer}(z) \simeq 0.02$ km^{-1} must be expected unless temperature and pressure data from a radiosonde ascent of a nearby weather service station are available. This error corresponds to ~10% in the case of aerosol measurements in the boundary layer or in cirrus clouds. The statistical error is of the same order of magnitude. It is thus possible to measure cirrus particle extinction properties with a relative error of 20% and with time and range resolutions of 5 to 20 min and 300 to 600 m, provided the scattering properties do not vary significantly. Multiple scattering contributes less than 10% at cloud base and of the order of 5% for the remaining cloud region.

B. Particle Backscatter Coefficient

In Fig. 3 a height profile of the particle-backscatter coefficient that is determined from the ratio of the elastic to the inelastic nitrogen Raman signal by using Eq. (4) is shown. In addition, the extinction coefficient, which is the same as in Fig. 1(a), and the

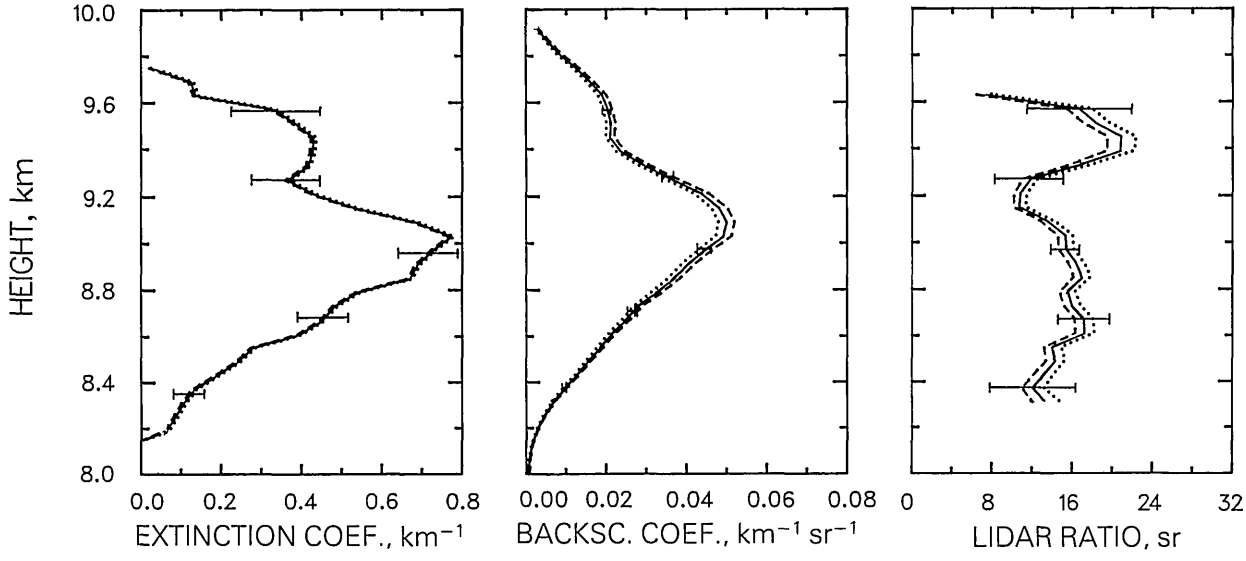

Fig. 3. Cirrus particle extinction and backscatter coefficients and the corresponding extinction-to-backscatter ratio for λ_0 = 308 nm, determined on 24 October 1989 between 1809 and 1821 lt. An ozone density profile according to the standard ozone model for midlatitude conditions is assumed in the case of the solid curve. The dotted and dashed curves are determined by assuming zero ozone density and an ozone concentration that is a factor of 2 higher than the standard model content, respectively.

resulting extinction-to-backscatter ratio profile are given.

In the determination of the backscatter coefficient the signals of each channel are averaged first. After correction of atmospheric effects such as the nitrogen density decrease and the difference of the atmospheric transmission for the laser and nitrogen Raman wavelengths between the reference height z_0 and the measurement height z [see Eq. (4)], the ratio of the averaged and corrected signals is formed and smoothed. The smoothed signal ratio profile is then used to calculate the backscatter coefficient according to Eq. (4). In Fig. 3, the same sliding average length of 300 m is selected as in Fig. 1(a) in the cirrus layer. Again a calculation step width of 60 m is chosen. The reference height is located at $z_0 = 6$ km, where particle extinction is low [see Fig. 1(a)]. For the backscatter boundary value, $\beta_{\lambda_0}^{\text{aer}}(z_0) = 0$ is chosen. A proportionality of particle scattering to λ^{-1} and λ^0 is assumed below and within the cloud, respectively. Radiosonde data of temperature and pressure are used for the estimation of air density and molecular scattering properties.

A relative systematic error of 5% to 10% that is due to realistic uncertainties of the estimated ozone density, temperature, and pressure profiles must be taken into account, if no radiosonde data are available and an ozone density profile according to the standard ozone model is assumed but the true ozone content is 0 or a factor of 2 higher than the standard model content. The influence of the ozone transmission estimate is shown in Fig. 3. The effect decreases with decreasing distance $z - z_0$ [see Eq. (4)]. It is therefore advisable to set the reference height as close as possible to the cloud base.

In the case of Fig. 3 the error of $\beta_{\lambda_0}^{\text{aer}}(z)$ that is caused by an uncertainty in the determination of the particle transmission ratio in Eq. (4) can be neglected. Aerosol transmission between the reference height $z_0 = 6$ km and the cloud base is approximately 1 at both wavelengths because of low particle extinction [see Fig. 1(a)]. The transmission ratio is ~ 1 within the cirrus because of negligible wavelength dependence of the extinction by ice crystals (see Section 3). The assumption of a weak wavelength dependence of the ice-crystal scattering was confirmed by a measurement of one lidar group during ICE'89.[17]

A proportionality of particle extinction in the cirrus to λ^{-1} instead of λ^0 would, in the case of Fig. 3, cause an error of the backscatter coefficient of less than 1%. But the wavelength dependence can play a much more important role in mixed clouds with high optical thickness that consist of small water droplets and large ice crystals, so that the wavelength dependence varies between λ^0 for ice crystals and λ^{-1} for water droplets. Studies of boundary-layer backscattering are another example of a case for which the influence of the wavelength dependence may not be negligible. k and thus λ^{-k} is different for different aerosol types.

The error of $\beta_{\lambda_0}^{\text{aer}}(z)$ that is due to the uncertainty of the particle reference value $\beta_{\lambda_0}^{\text{aer}}(z_0)$ is assumed to be small in Fig. 3 because the extinction profile shown in Fig. 1(a) suggests a scattering ratio $\beta_{\lambda_0}^{\text{aer}}/\beta_{\lambda_0}^{\text{mol}} \simeq 0$ at the reference height $z_0 = 6$ km. As was mentioned, $\beta_{\lambda_0}^{\text{aer}}(z_0)/\beta_{\lambda_0}^{\text{mol}}(z_0) \leq 0.01$ for $\lambda_0 = 308$ nm under typical air conditions for the upper troposphere.[25] However, a relative error of $\sim 10\%$ occurs if the true reference backscatter ratio $\beta_{\lambda_0}^{\text{aer}}(z_0)/\beta_{\lambda_0}^{\text{mol}}(z_0) = 0.1$ instead of 0.

Multiple scattering will not affect the determination of the backscatter coefficient in high-altitude clouds, after Eq. (4). Strong forward scattering by ice crystals or droplets leads to an increase of cloud transmission. This effect is ratioed out by applying Eq. (4).

As in the case of the extinction-coefficient determination, an additional error of considerable magnitude can be introduced into the calculation of the backscatter coefficient if particle scattering properties vary strongly during the signal sampling and averaging time period Δt. Here the error of the measurement results from the fact that the signals $P_{\lambda_0}(t)$ and $P_{\lambda_R}(t)$, where t denotes the time, are averaged instead of the signal ratio $P_{\lambda_0}(t)/P_{\lambda_R}(t)$. When elastic-backscatter signals are averaged, products of a variable backscatter coefficient with a variable transmission are averaged [see Eq. (1)]. The (true) mean backscatter coefficient is obtained only if the mean elastic-backscatter signal is equal to the product of the mean values of the backscatter coefficient and the transmission term $\overline{\beta T^2}$, i.e., if the sum of the products of $\beta'(t)T'^2(t)$, where $\beta'(t)$ and $T'(t)$ are expressed by $\beta(t) = \overline{\beta} + \beta'(t)$ and $T(t) = \overline{T}T'(t)$, is equal to 0.

Our theoretical analysis and simulation studies show that the averaging effects on the backscatter coefficient and on the extinction coefficient, as presented in Fig. 2, deviate by no more than a few percent if a constant relation $S_{\lambda_0}^{\text{aer}}$ between extinction and backscattering is assumed. Thus, starting from Fig. 2(a), calculating the elastic-backscatter and Raman signals after Eqs. (1) and (2) with a constant lidar ratio, separately averaging the signals for the different channels, and, finally, determining the backscatter coefficient after Eq. (4) will produce approximately the same profiles for $\beta_{\lambda_0}^{\text{aer}}(z)$ and $\delta\beta_{\lambda_0}^{\text{aer}}(z)$ as those of $\alpha_{\lambda_0}^{\text{aer}}(z)$ and $\delta\alpha_{\lambda_0}^{\text{aer}}(z)$ in Figs. 2(c) and 2(d). According to Fig. 2, the sum of the products $\beta'(t)T'(t)$ is negligible for only the region below the simulated cloud layer.

Large errors can be avoided by calculating the backscatter coefficients separately for the periods Δt_1 and Δt_2 and averaging the obtained values. Theoretically the averaging of the signal ratios could lead to the correct solution, provided that the signals can be stored with sufficient time resolution and that the signal-to-noise ratio of the raw data is high. In practice, the signal-to-noise ratio is low, especially for the Raman signals, and the same considerations as those developed in Subsection 4.A for the extinction coefficient also apply to the determination of backscatter coefficients.

In conclusion, again nearly constant optical proper-

ties or, under variable atmospheric conditions, optical depth values below 0.5 are needed during the signal averaging period Δt in order to avoid relative errors larger than 20%. The combined effect of uncertainties in ozone density, temperature, and pressure on backscatter coefficient profiles may result in a relative error of 10%. The reference height should be set just below the cloud to minimize the error from the uncertainty in the estimates of the molecular and particle transmissions between z_0 and the measurement height z. A relative statistical error of less than 10% in combination with high depth resolution can be achieved only in regions of strong backscattering, i.e., in clouds and in the boundary layer.

C. Lidar Ratio

The atmospheric input parameter that most affects the solution of Eq. (5) is the ozone density. An underestimation of the ozone content leads to an overestimation of the particle extinction coefficient [which is the numerator in Eq. (5)] and an underestimation of the backscatter coefficient [which is the denominator in Eq. (5)] and vice versa. In the case of cirrus observations, the error of the lidar ratio that is due to the ozone uncertainty is of the order of 5% to 10% (see Fig. 3). An additional 5% can occur if standard atmosphere profiles for the temperature and pressure are assumed, i.e., if no actual radiosonde data are available.

The analysis in Subsections 4.A and 4.B shows that the error from uncertainties in the estimate of the particle wavelength exponent k used in Eqs. (3) and (4) and of the reference value $\beta_{\lambda_0}^{\text{aer}}(z_0)$ used in Eq. (4) can be neglected in the case shown in Fig. 3. The multiple-scattering effect is the same as for the extinction coefficient, i.e., between 5% and 10%.

Rapid temporal changes of the aerosol extinction properties do not affect the determination of $\overline{S_{\lambda_0}^{\text{aer}}}$ if the lidar ratio is constant during the measurement interval because then $\delta\beta/\beta \simeq \delta\alpha/\alpha$ (see Subsection 4.B). If both the lidar ratio and the particle extinction coefficient vary, the measured lidar ratio is determined mainly by the periods of strong particle scattering, as the simulations and the evaluation of the lidar data show. Assuming, e.g., in Fig. 2 a lidar ratio of 10 instead of 20 sr within the cloud layer during Δt_2, we obtain a lidar ratio for the total time Δt of ~10 sr at the bottom and 12.5 sr at the top of the cloud instead of the mean value of 15 sr. It can thus be concluded that varying optical properties do not significantly affect the determination of cloud lidar ratios. For the case shown in Fig. 3 and also for the measurements presented in Subsection 4.D no significant errors are introduced by signal and signal ratio smoothing.

A critical point in the error analysis is the estimation of the influence of specular reflection by falling ice crystals that are horizontally oriented. Whereas small particles have no preferred orientation, crystals of typical cirrus particle size sink with their longest axes parallel to the ground.[32] Horizontal alignment gives the maximum resistance of motion. Large particles begin to oscillate. A persistent fluttering occurs. Crystals oriented precisely horizontally cause a large backscatter signal by specular reflection. Few oriented crystals are believed to be able to produce strongly enhanced backscattering and a low lidar ratio.[33] If this is true, specular reflection, often observed in cirrus with a vertically pointing lidar,[34] will dominate all experimentally determined lidar ratio values. However, recent measurements performed with our lidar tilted by 28 mrad do not confirm this assumption, as a tilt angle of greater than 5 mrad should be sufficient to ensure that no specular reflection affects the lidar results.[34] Again extinction-to-backscatter ratios between 5 and 20 sr were observed in most cases. Only in a few exceptional cases were large lidar ratios > 30 sr, which are assumed to be caused by specular reflection, determined with the tilted system. If the lidar is tilted, photons backscattered from horizontally oriented crystals cannot enter the receiver telescope. So we believe that specular reflections do not play that important a role. At least, in many measurement cases, scattering properties of randomly oriented particles are measured with the vertically pointing combined lidar.

In summary, the combined lidar permits the determination of the lidar ratio with a relative statistical error of 15% to 30% and a range resolution of 300 to 600 m in high-level clouds. Compared with the influence of varying optical properties during the signal averaging time on $\alpha_{\lambda_0}^{\text{aer}}$ and $\beta_{\lambda_0}^{\text{aer}}$, the effect on $S_{\lambda_0}^{\text{aer}}$ is small. The most important atmospheric input parameter is the ozone density profile. The total relative systematic error is of the order of 10% to 20%.

D. Particle Extinction Coefficients from Klett's Inversion Method

A large number of papers have been published in which the error of the Bernoulli solution for the particle extinction coefficient is analyzed (see, e.g., Klett,[8,35] Fernald,[9] and Bissonnette[36]). The discussion of the applicability of the Klett inversion procedure to cloud investigations will, therefore, be restricted here to aspects that have not been sufficiently considered until now. Extinction profiles obtained with the inversion method [Eq. (6)] and the Raman method [Eq. (3) or Eq. (7)] are presented for two cases, one with a nearly height-independent extinction-to-backscatter ratio (in this section) and one with a range-dependent lidar ratio (in Section 5).

In general, great care must be taken in the interpretation of the Bernoulli solution for the particle extinction coefficient. As is well known in the lidar community, the inversion method suffers from the fact that two physical quantities, the particle backscatter and the particle extinction coefficients, must be determined from only one measured lidar signal. To solve Eq. (6), we must make assumptions about the relation between the two, and we need an esti-

mate of the boundary value of the aerosol extinction coefficient. These data, $S_{\lambda_0}^{aer}(z)$ and $\alpha_{\lambda_0}^{aer}(z_0)$, are usually hard to assess and can cause large uncertainties in the aerosol extinction coefficient.

Most devices designed as backscatter lidars have been operated in the visible and the infrared parts of the spectrum. UV devices offer a big advantage in that the correct estimate of the boundary value, at least at the far end of the lidar range, is much easier to obtain because of strong Rayleigh scattering. On the other hand, a drawback of a system measuring at 308 nm is the onset of UV ozone absorption at this wavelength. A relative error of more than 20% must be faced under unfavorable conditions for the cirrus particle extinction coefficients owing to the uncertainty in the estimate of the ozone optical depth between the reference height z_0 and z (see Section 3). The effect is minimized if z_0 is close to the cloud base. The ozone influence is much more important here than in the determination of $\alpha_{\lambda_0}^{aer}$ from the Raman signals because the round-trip absorption at 308 nm is so much larger than the additional absorption of the 332-nm Raman backscatter radiation.

The remaining problem is the estimation of the lidar ratio. Depending on aerosol type, $S_{\lambda_0}^{aer}$ can vary over orders of magnitude. In practice, no information on the required height profile of the lidar ratio is usually available.

An average value of the lidar ratio can be obtained in the case of sufficiently constant microphysical cloud conditions in both space and time. A trial value is taken for the lidar ratio, and Eq. (6) is solved by forward integration. If the solution is unstable, another, lower trial value is used until a stable solution results. The same trial value is then used for the backward integration of Eq. (6). Normally the resultant profiles of the extinction coefficient will differ. The trial value can then be varied until the results of the forward and backward integration coincide to the desired degree of accuracy. Usually ~ 5 iteration steps provide a sufficiently good lidar ratio, and two iterations will probably suffice as soon as some experience in the use of the technique has been gained. The procedure is illustrated in the profiles of Fig. 4, which show the behavior of the forward and the backward integrations for trial values that are too small [Figs. 4(a) and 4(b)], almost right [Fig. 4(c)], and too large [Fig. 4(d)]. If signals from above the cloud are not available, the sensitivity of the forward integration solution to the lidar ratio estimate alone can be used to find the most reliable lidar ratio.[37] This method is discussed in more detail in Section 5.

The optimum average lidar ratio of $S_{\lambda_0}^{aer} = 15.7$ sr, for which the solutions of forward and backward integration approximately coincide, is taken in the case of Fig. 5. In Figs. 4 and 5 forward integration ($z > z_0$) starts at $z_0 = 6$ km, and backward integration ($z < z_0$) starts at $z_0 = 12$ km above the tropopause; both reference heights could be chosen so that they coincide with layers of low particle scattering. The

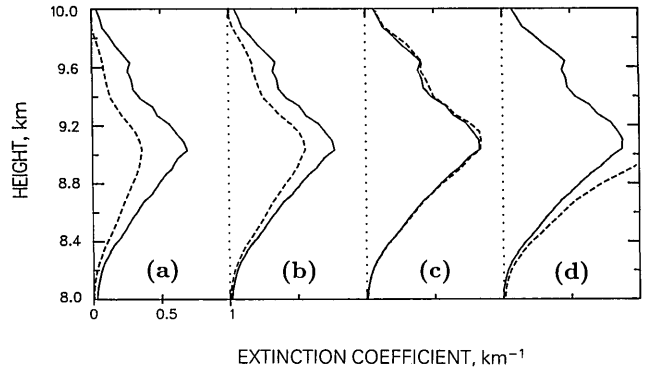

Fig. 4. Bernoulli solutions obtained by applying forward (dashed curve) and backward integration (solid curve) and by assuming a range-independent lidar ratio of $S_{\lambda_0}^{aer}$ = (a) 10, (b) 13, (c) 16, and (d) 19 sr. The measured elastic-backscatter data are the same as those in Fig. 3.

boundary values $\alpha_{\lambda_0}^{aer}(z_0)$ were set to 0 in both cases. The molecular scattering coefficients needed to solve Eq. (6) are calculated with actual data of temperature and pressure obtained from a radiosonde ascent. Before the inversion method is applied, the signal profile, corrected for ozone absorption, is smoothed with a sliding average window length of $\Delta z = 300$ m. The calculation step width is 60 m. For comparison, in Fig. 5 the extinction profile determined from the inelastic nitrogen Raman signal profile (dotted curve, see also Fig. 3) is shown. The value of $S_{\lambda_0}^{aer} = 15.7$ sr agrees well with the average lidar ratio of ~ 15.5 sr, which is determined with the Raman method as shown in Fig. 3. The small difference between the extinction coefficient obtained for the upper cirrus region with the Klett and the Raman lidar method in Fig. 5 is caused mainly by the slight variations of the lidar ratio. The strong influence of the depth variability of $S_{\lambda_0}^{aer}(z)$ on the Bernoulli solution is discussed in detail in Section 5. It is shown there that, even if the best-available, but

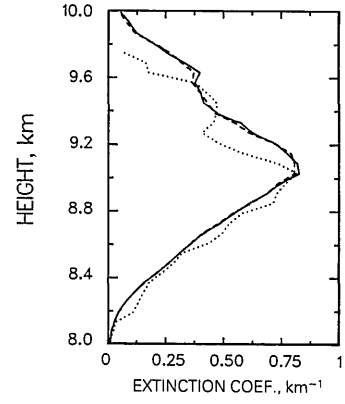

Fig. 5. Particle extinction coefficient determined by the inversion method [Eq. (6); near-end solution, dashed curve; far-end solution, solid curve] for the optimum range-independent lidar ratio $S_{\lambda_0}^{aer}$ = 15.7 sr. For this extinction-to-backscatter ratio the near- and remote-end solutions coincide approximately. The particle extinction profile derived from the Raman signals is shown for comparison (dotted curve, see Fig. 3).

height-independent, lidar ratio is used, large uncertainties in the particle extinction profile remain.

An additional aspect must be discussed here that has not, in the authors' opinion, been sufficiently considered in the Klett error analysis until now. As in Subsections 4.A and 4.B, a significant error can be introduced into the calculation if the scattering properties vary strongly during the signal sampling and averaging time period Δt. This is demonstrated in Fig. 6.

The error results from the fact that the elastic-backscatter signal depends on a variable backscatter coefficient β and a variable transmission term T^2 [see lidar equation (1)]. Let β and T be expressed here as $\beta(t) = \bar{\beta} + \beta'(t)$ with the mean value $\bar{\beta}$ and the deviation $\beta'(t)$ and $T(t) = \bar{T}T^*(t)$, where $\bar{T}$ is the transmission corresponding to the mean optical depth for the time period Δt, from which the desired extinction coefficient can be determined, and $T^*(t)$ is used to describe the deviation of $T(t)$ from $\bar{T}$. The true mean particle extinction coefficient [Fig. 6(c), dotted curve] is then obtained if the average of $\beta'(t)T^{*2}(t)$ is equal to 0. This is approximately the case in Fig. 6 below and above the layer of strongly varying particle extinction conditions. The value of $|\overline{\beta'(t)T^{*2}(t)}|$ and, thus, the error of the Klett solutions increase with height.

As stated above large errors as shown in Fig. 6 may not play an important role in studies of optically thin cirrus clouds as long as rapid and large variations of the optical depth are absent, but must be taken into account in measurements in inhomogeneous water clouds in which the particle extinction coefficient can vary between values near 0 and 30 km^{-1} within a few seconds.

In summary, the error of the Bernoulli solution in terms of the particle extinction coefficient can be large because of the large uncertainty of the estimate for the lidar ratio $S_{\lambda_0}^{aer}$ in Eq. (6). If both the forward and the backward integration variant of the Klett method can be applied, which usually holds for optically thin clouds, and the near- and far-end boundary values are well estimated, an appropriate average lidar ratio can be determined and the error in the determination of $\alpha_{\lambda_0}^{aer}(z)$ can be minimized. At 308 nm, a good calibration is possible because of strong Rayleigh scattering. On the other hand, a good estimate of ozone absorption is required. As in the case of the Raman lidar, care must be taken in the study of inhomogeneous clouds.

An advantage of the Klett method over the Raman lidar method is the fact that particle scattering is determined from a strong elastic-backscatter signal that is several orders of magnitude larger than the

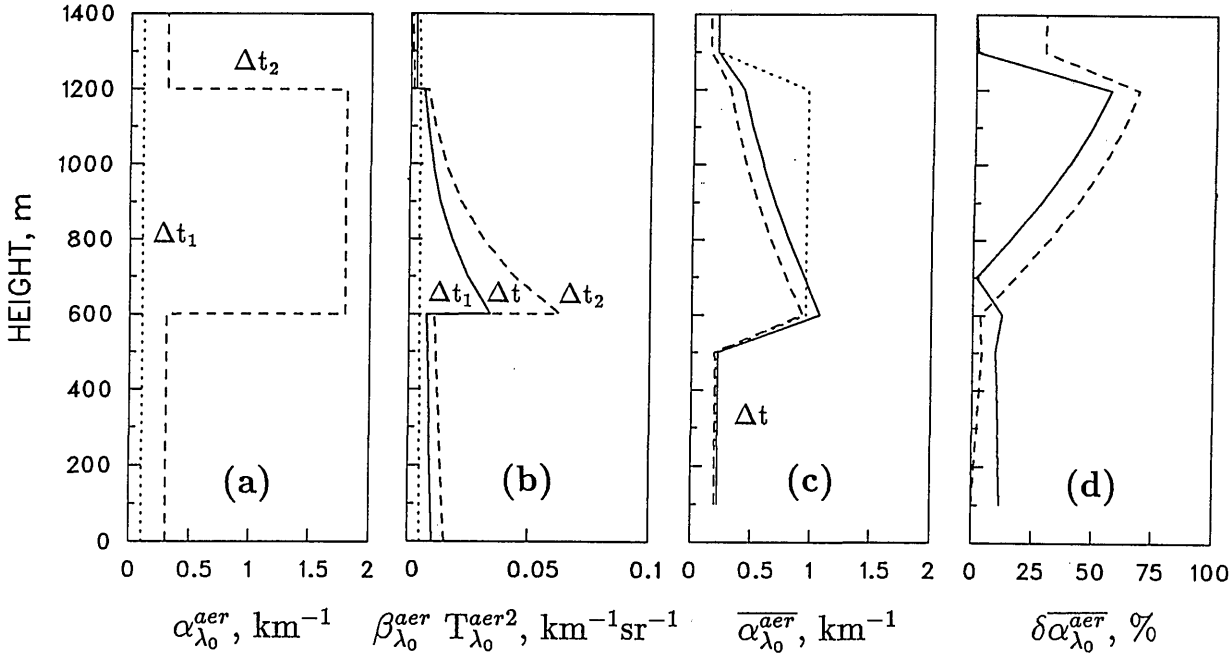

Fig. 6. Modeled particle extinction coefficients determined from elastic-backscatter signals measured during a time period of strongly varying particle extinction conditions. (a) Assumed particle extinctions during the first (dotted curve) and second (dashed curve) halves of the total sampling period $\Delta t = \Delta t_1 + \Delta t_2$. For simplicity, molecular scattering and extinction are neglected. (b) Range-corrected elastic-backscatter signal assuming $K_{\lambda_0}O(z) = 1$ in the lidar equation (1). The profiles for the time sections Δt_1 (dotted curve) and Δt_2 (dashed curve) are calculated with the extinction coefficients shown in (a) and an aerosol lidar ratio of 20 sr. The solid curve is obtained by averaging the profiles for Δt_1 and Δt_2. (c) Particle backscatter coefficient determined from the mean corrected signal profile [(b), solid curve] by using the Klett method in the forward (dashed curve) and backward (solid curve) integration mode. The reference heights are $z_0 = 100$ m (forward integration) and 1400 m (backward integration). The correct boundary value of 0.2 km^{-1} and the correct lidar ratio are taken for the retrieval. The calculation step width is $\Delta z = 100$ m. The corresponding true mean extinction profile according to (a) is shown for comparison (dotted curve). (d) Relative error of the particle extinction coefficients derived by applying forward (dashed curve) and backward (solid curve) integration.

Raman signal. The Klett method can thus be applied during the daytime. The statistical error from signal noise is small, and high temporal and spatial resolution can be achieved. The influence of variable scattering conditions during signal averaging periods is reduced by the possibility of short averaging intervals.

5. Experimental Results and Discussion

In this section examples of independent measurements of the extinction and backscatter profiles in high-altitude clouds and, thus, of the lidar ratio profile are presented and discussed. Based on another comparison of the Bernoulli with the Raman lidar solution and on the results of a cirrostratus measurement, the applicability of the Klett inversion method to cloud studies is illustrated.

The results shown in the figures below have been obtained with the combined Raman elastic-backscatter lidar. The statistical error, which is due to photon noise, and, in the case of lidar ratio observations, the systematic error resulting from the uncertainity in the assumed ozone density (see Section 4) are indicated by error bars and dashed curves, respectively. Other systematic errors can be neglected here, especially since the temperature and pressure profiles were measured with radiosondes launched at the lidar station. Layers of low particle scattering were present below the cloud in all cases shown. This justifies the use of the reference value $\beta_{\lambda_0}^{aer}(z_0) = 0$ and the neglect of the error introduced by $\delta\beta_{\lambda_0}^{aer}(z_0)$. The calculation step width is 60 m.

In Fig. 7, a cirrostratus measurement is shown. The atmospheric conditions on that day were unique during the field campaign of ICE'89 in that optical and geometric properties of the cloud deck remained approximately unchanged with time and height for more than 3 h. Only in this particular case could the average of a 2-h measurement be taken without making a large error. Most of the 2-min average values of the cloud optical depth, derived from the respective high-resolution Raman signal profiles, are between 0.2 and 0.5. According to the discussion in Subsections 4.A and 4.B, the extinction and backscatter coefficients shown in Fig. 7 are estimated to be less than 10% and 20% too small for the lower cloud region and the main cloud layer between 10.5 and 11.6 km in height, respectively, despite the long averaging time.

The cloud temperatures range from −38°C at 9 km to −58°C at the top of the cirrus, which coincides with the tropopause. The similarity of the extinction and backscatter profiles suggests a close relation between the mean transmission and reflection properties. The mean optical depth, derived from the extinction coefficient, is 0.38. Taking into account the effects of smoothly changing extinction conditions and multiple scattering (5% to 10%, see Section 4), we obtain a single-scattering optical depth of the order of 0.5.

The vertical distribution of the lidar ratio suggests different microphysical characteristics in the lower and upper parts of the cloud. However, the interpretation of the experimentally determined extinction-to-backscatter ratios is difficult because of the large errors, as indicated in Fig. 7, of the unknown influence of specular reflection and of the range dependence of multiple scattering, which is also unknown.

Nevertheless, there are two good reasons to believe that the measured data are typical for cirrus scattering conditions, i.e., scattering by mainly randomly oriented crystals. First, our recent cirrus measurements with a tilted lidar show, in most cases, no significant differences in the results obtained under zenith angles of < 1 mrad and 28 mrad. Second, and more important, the determined lidar ratios agree well with theoretical values inferred from numerical

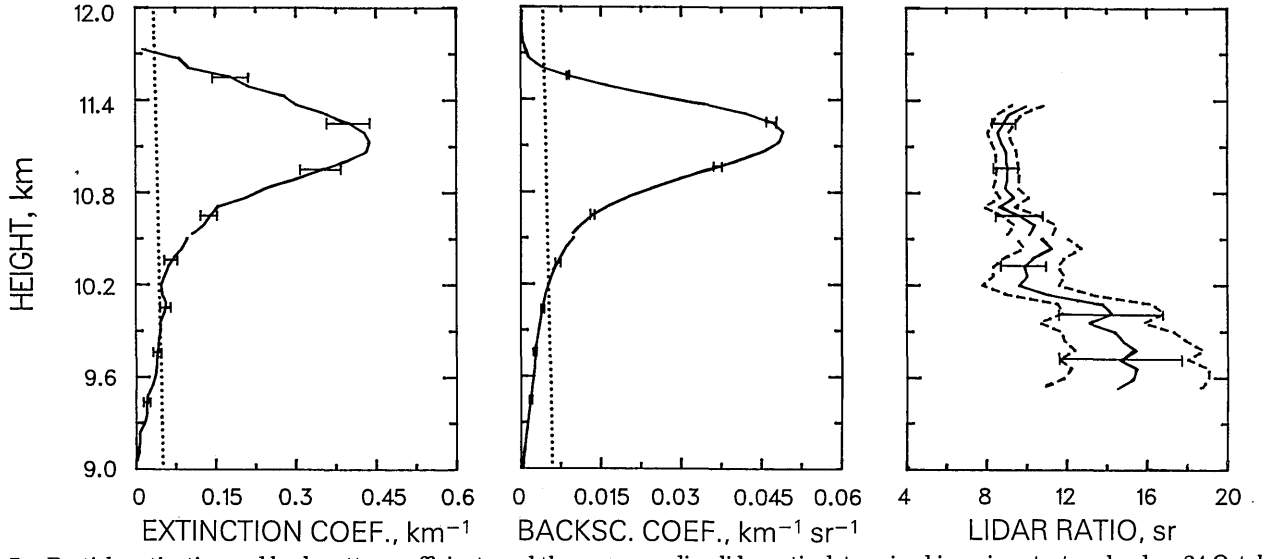

Fig. 7. Particle extinction and backscatter coefficients and the corresponding lidar ratio determined in a cirrostratus cloud on 24 October 1989 between 1854 and 2042 lt. 725,600 laser shots are averaged. Signal smoothing lengths are $\Delta z = 600$ m for $z < 10.5$ km and 300 m for $z \geq 10.5$ km. Rayleigh extinction and backscatter coefficients (dotted curves) are shown for comparison.

calculations[30] in which, for observed ice-crystal size distributions of a cirrostratus,[38] cold (−55°C) and warm (−30°C) cirrus clouds,[39] and a cirrus uncinus cloud[38] with a considerable amount of large ice crystals with lengths >500 μm, the scattering phase function was determined for λ = 550 nm with the assumption of randomly oriented hexagonal ice crystals. According to these calculations the lidar ratio is ~10 sr for typical cirrus clouds, including cirrostratus, and 17 sr for cirrus uncinus, i.e., for an ice cloud with more larger particles. The scattering phase function for randomly oriented and small hexagonal plates (diameter, 20 μm) and columns (length, 120 μm) and a wavelength of λ = 632 nm yields a lidar ratio between 5 and 10 sr.[40]

It must be stated here that this is, to our knowledge, the first time that experimentally derived lidar ratios agree in a satisfactory way with results of theoretical studies. Mean cloud lidar ratios between 30 and 80 sr, frequently >40 sr, were obtained with the so-called lidar and infrared radiometric (LIRAD) method.[41,42] During FIRE'86, mean cloud lidar ratios between 15 and 50 sr, frequently between 25 and 35 sr, were determined by the use of the HSRL technique.[13] None of these attempts to reproduce experimentally the small lidar ratio values of the models was successful.

It is unclear at the present time how much of these discrepancies may be caused by the fact that, in numerical calculations, crystals are modeled simply by hexagonal plates and columns, or spheres. Assemblies of real ice crystals, however, contain partly complex shapes, depending on water vapor pressure, which increases with temperature, and on the strength of vertical motions at different scales in the upper troposphere. Results of numerical calculations of the extinction-to-backscatter ratio for ice clouds composed of irregularly shaped ice particles such as bullet rosettes would be useful for clarifying the differences between model and experimental results. Ideally shaped crystals, as assumed in the models, are possibly more frequently present in cirrus clouds at higher latitudes (>50°N or S) where convective processes may be relatively weak compared with those in tropical and lower midlatitude regions. ICE'89 took place in the German Bight of the North Sea at >53°N. FIRE'86 and other lidar ratio measurements were performed near 40°N and S or at lower latitudes.

The numerical studies imply a decrease of the lidar ratio with a decreasing size of scattering ice crystals. The lidar ratio profile in Fig. 7 may thus indicate the presence of smaller particles in the layer of strong backscattering and larger particles in the layer below. Evaporation of ice crystals in the fall-streak region below 10.5 km must also be taken into account. Laboratory studies[43] show that the corners of particles become rounded during evaporation, and particles probably change their scattering properties. Comparisons with studies of scattering properties of droplets[44,45] indicate that spheres with diameters within the atmospheric range between 0.1 and 100 μm exhibit a larger lidar ratio, between 15 sr and 60 sr, than hexagonal crystals of atmospheric ice clouds. Breakup was found to take place when the relative humidity drops below 70% related to ice.[43] In this way, many small particles that cause a lowering of the lidar ratio may be produced.

With respect to cirrus studies with an elastic-backscatter lidar, the above discussion makes clear that a range-variable lidar ratio must generally be taken into account if the Klett method is applied, whether or not specular reflection is present. The error introduced in the Bernoulli solution by a range-independent extinction-to-backscatter ratio is discussed below.

How specular reflection influences the extinction-to-backscatter ratio can be seen in Fig. 8. The measurement was performed in the last of several cirrus bands crossing the lidar station in a weak southwesterly airflow. Temperatures between −25°C and −40°C were measured by radiosonde between 7 and 9 km. The optical depth of the cirrus is estimated to be again ~0.5 ± 0.1.

As can be seen, a nearly range-independent extinction coefficient is found, whereas the backscatter coefficient increases with height, with a strong maximum in the upper cirrus region. The corresponding profile of the lidar ratio shows typical cirrus values for heights below 8 km, a sharp decrease at about 8 km, and extremely small values of 2 to 3 sr in the upper cloud region, which are presumably caused by a layer with a considerable amount of horizontally oriented ice crystals. This result is in agreement with numerical calculations.[33] Such low lidar ratios cannot be explained by multiple scattering, which affects the results by ~10% only. The large lidar ratio values at the bottom of the cloud may result from the presence of large crystals, ice spheres, or supercooled water droplets. The temperature at 7 km in height was only −25°C. Water droplets, possibly present in cirrus clouds at temperatures >−40°C,[46] lead to an increase of the lidar ratio. The deviation of the extinction from the backscatter profile in the case of Fig. 8 clearly demonstrates that the reflection properties of cirrus clouds depend quite significantly on whether the ice crystals are oriented randomly or in a horizontal plane.[47] Particle number density appears to be nearly constant with height in the present case because the extinction coefficient, which is primarily a function of particle density, is almost range independent.

Figure 9 shows two measurements of an inhomogenous cirrus deck that remained after the passage of a cold front. A fibrous cloud covering the entire sky and consisting of long ice-crystal streamers and filaments could be observed in the moonlight. Strong winds were present in the upper troposphere. Temperatures ranged between −36°C at 7.5 km and −41°C at the top of the cirrus layer at 8.5 km. Because of rapidly varying scattering and extinction conditions during the measurement, the relative er-

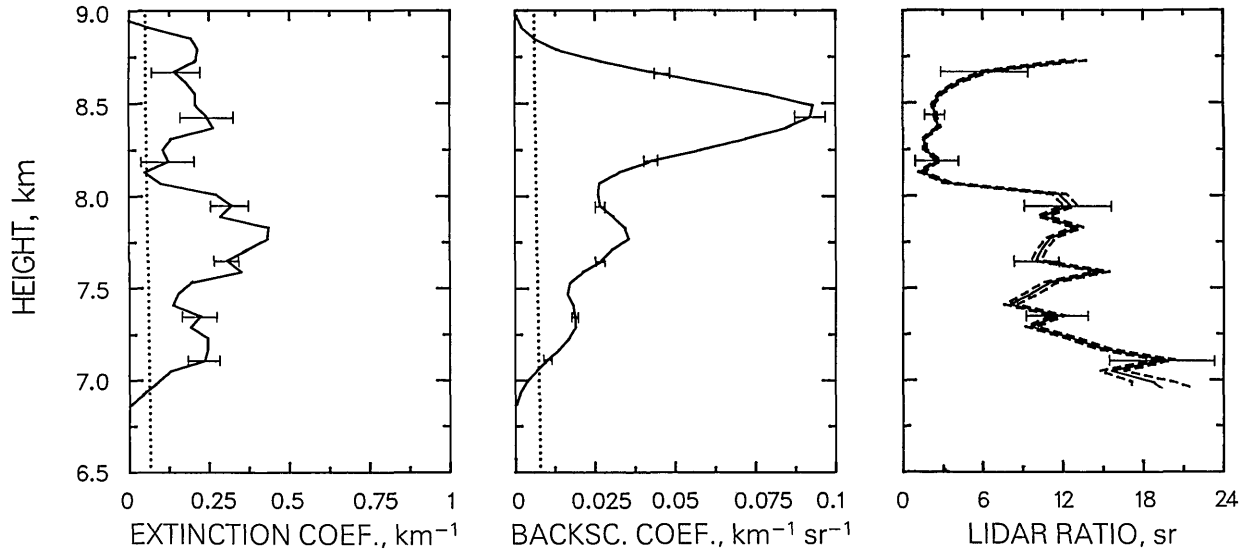

Fig. 8. Cirrus scattering properties determined with a combined lidar in a cirrus cloud on 20 September 1989 between 0447 and 0456 lt. 98,358 laser shots are averaged. Signal smoothing length is Δz = 300 m. Profiles of Rayleigh extinction and backscattering (dotted curves) are also plotted.

ror of $\beta_{\lambda_0}^{aer}(z)$ may be larger than 20%. The error introduced by the uncertainty in the ozone density estimate, not shown in Fig. 9, is of the same order as that shown in Fig. 8.

The two measurements were taken within 30 min. In the phase of weak backscattering, a lidar ratio of ~5 sr was measured. For strong backscattering, ~10 min later, a lidar ratio of greater than 10 sr was found. According to the profiles of $\beta_{\lambda_0}^{aer}$ and $S_{\lambda_0}^{aer}$, the extinction coefficient ($\alpha = S\beta$) increases with time by a factor of ~4, while the backscatter coefficient increases by only a factor of 2. The examples again illustrate that care must be taken when extinction properties are inferred from elastic-backscatter data alone, with the assumption of a time-invariant and range-independent lidar ratio. In Fig. 9, the typical range of cirrus lidar ratios measured during the ICE'89 campaign is presented. Extinction-to-backscatter ratios between 5 and 15 sr were usually observed.

Finally, in Fig. 10, a measurement in a water cloud (altostratus) is shown for comparison. Since the lidar system was optimized for the observation of high clouds, only a few water cloud cases could be found. In addition, strong extinction often prevents a measurement of the Raman signal profile within the cloud.

The measurement was performed in the late evening of 24 October in a stable and homogenous altostratus cloud with an optical depth of ~2 and a mean temperature of −8°C. The optical depth varied between 0.6 and >2 during the passage of the altostratus cloud field. A relative error of the order of 50% must be taken into account for $\alpha_{\lambda_0}^{aer}$ (see Subsection 4.A). The influence of varying optical properties on

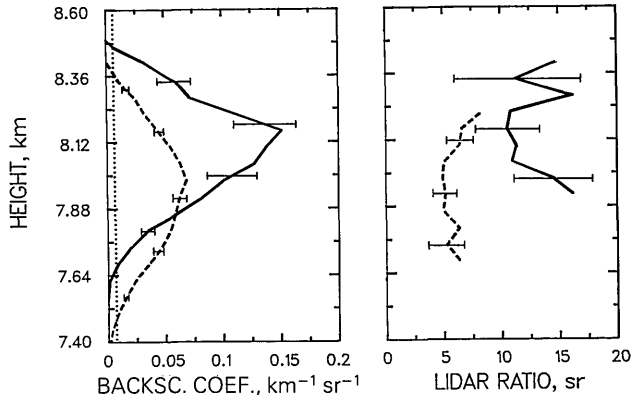

Fig. 9. Particle backscatter coefficient and extinction-to-backscatter ratio determined in a cirrus cloud on 13 October 1989 at 2119 (dashed curves) and 2138 lt (solid curves). 107,099 and 21,528 laser shots sampled in 10 min and 2 min are averaged, respectively. The data smoothing length is Δz = 360 m. The Rayleigh backscatter coefficient is given by a dotted curve.

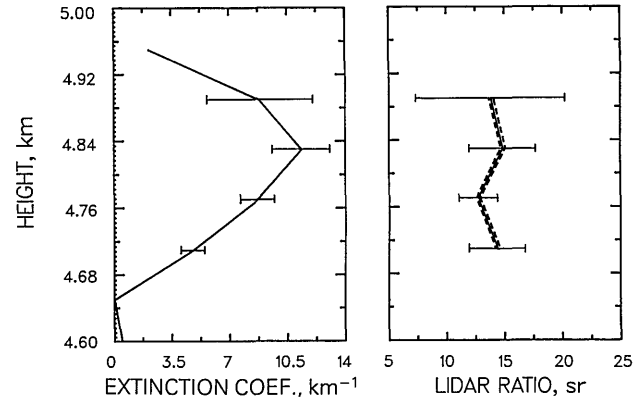

Fig. 10. Particle extinction coefficient and extinction-to-backscatter ratio determined in an altostratus cloud on 24 October 1989 at 2225 lt. 18,140 laser shots sampled in 2 min are averaged. Spatial resolution is 60 m. The comparably small Rayleigh extinction coefficient is given by the dotted curve.

the lidar ratio are estimated to be small (see Subsection 4.C).

The lidar ratio profile agrees sufficiently well with results obtained in laboratory measurements for realistic atmospheric droplet spectra. In one study[44] lidar ratios between 17 and 19 sr were found for polydisperse clouds with a broad spectrum of droplet sizes and for a measurement wavelength of $\lambda = 632$ nm. From another study[45] at $\lambda = 514$ nm it can be concluded that the lidar ratio is between 15 and 23 sr for atmospheric water clouds of low optical depth and correspondingly low extinction coefficients, as is the case in Fig. 10. Also, a decrease of the extinction-to-backscatter ratio with increasing droplet size was found.[45] Keeping in mind that our measurements were performed at $\lambda = 308$ nm, that the laboratory analysis also suggests a decrease of the lidar ratio with decreasing wavelength for a given droplet spectrum, and, finally, that a small multiple-scattering effect must be taken into account in lidar measurements in high altitude water clouds even for small RFOV's, which also leads to a decrease in the lidar ratio, we find that the measured cloud extinction-to-backscatter ratios agree well with the laboratory results.

In the last part of this section, the applicability of the Klett inversion method to studies of cirrus optical properties is illustrated. It is shown that, although the extinction-coefficient profile can be incorrect because of the unrealistic assumption of a range-independent lidar ratio, the determined backscatter-coefficient profile, the cloud optical depth, and the mean cloud extinction-to-backscatter ratio can still be obtained with high temporal resolution and acceptable accuracy.

In Subsection 4.D a first comparison of extinction profiles obtained with Eq. (6) (the Bernoulli solution) and Eq. (3) or Eq. (7) (Raman lidar solution) for the case of a nearly range-independent extinction-to-backscatter ratio was shown (see Fig. 5). The agreement was good. In Fig. 11, a second comparison is presented for the case of a strongly range-dependent lidar ratio $S_{\lambda_0}^{aer}(z)$. The measured elastic-backscatter data are the same as those of Fig. 8. The optimum range-independent lidar ratio of 7.3 sr for which the solutions of backward (solid curve) and forward (dashed curve) integration nearly coincide is selected. The near-end ($z_0 = 6.4$ km) and remote-end ($z_0 = 9.4$ km) boundaries of the integration are set into regions with dominant Rayleigh scattering [$\alpha_{\lambda_0}^{mol}(z_0) \gg \alpha_{\lambda_0}^{aer}(z_0)$] so that the errors of the boundary values are assumed to be small. Before the inversion technique is applied, ozone absorption effects are corrected, and the corrected signal profile is smoothed with a gliding average window length of $\Delta z = 300$ m. The ozone optical depth is 0.03 for $\lambda_0 = 308$ nm between the two reference heights according to the standard ozone model. Thus, considering an ozone uncertainty of $\pm 100\%$ as before, we get a relative error of the extinction coefficient and of the particle optical depth of the order of 10%.

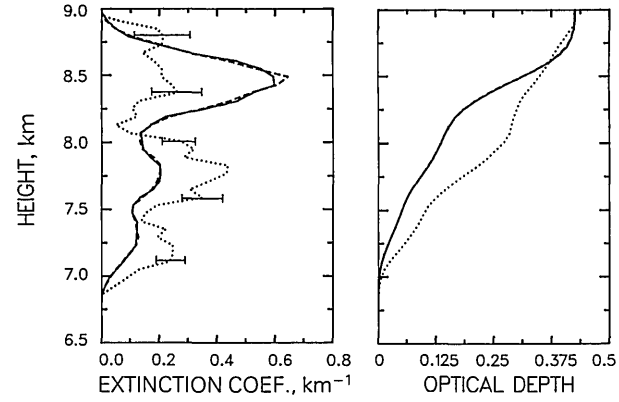

Fig. 11. Particle extinction coefficient (right) and resulting optical depth (left) determined from the elastic-backscatter signal at 308 nm by using the Klett method in the forward (dashed curve) and backward integration mode (solid curve). The measured data are the same as those in Fig. 8. A range-independent lidar ratio of $S_{\lambda_0}^{aer} = 7.3$ sr is assumed. For this lidar ratio the near-end and far-end solution coincide approximately. For comparison (dotted curves) the particle extinction profile and the corresponding optical depth determined after the Raman lidar method are also shown.

No similarity of the Bernoulli and the Raman lidar solutions can be seen. This is due to the strong variation of the lidar ratio with height (see Fig. 8). Only with $S_{\lambda_0}^{aer}(z)$ shown in Fig. 8 would the correct solution follow. By using a range-independent lidar ratio (and an alternative to this assumption is not available) we find that the obtained profile of the extinction coefficient is similar only to the backscatter coefficient profile in Fig. 8. The reason is that in cases of weak attenuation, the elastic-backscatter signal, corrected for range and molecular absorption and scattering effects, is mainly a function of the particle backscatter coefficient [see Eq. (1)].

Figure 11 underlines that reliable height profiles of the extinction coefficient cannot be determined with the Klett method. Only the profile of the backscatter coefficient is acceptable. On the other hand, the application of both forward and backward integration yields the mean cloud lidar ratio of $S_{\lambda_0}^{aer} = 7.3$ sr (see Fig. 8) along with the mean optical depth of the cloud of 0.42. We should mention that the technique is equivalent to the method in which the cirrus optical depth is determined from the Rayleigh backscatter signals from below and above the cloud and used to constrain a Bernoulli solution to the extinction profile, the range-independent lidar ratio, and the backscatter coefficient profile.[13]

Figure 12 illustrates the variability of the mean cloud lidar ratio with time and, again (see Fig. 4), the sensitivity of the solution of forward integration to the $S_{\lambda_0}^{aer}$ estimate. A short section of a cirrostratus measured on 18 October 1989 is selected. The reference heights of forward and backward integration are set to $z_0 = 6$ and 12 km (above the tropopause), respectively; $\alpha_{\lambda_0}^{aer}(z_0) = 0$ is taken. The calculation in Fig. 12 is performed with the lidar ratio $S_{\lambda_0}^{aer} = 13$ sr. This value is appropriate for the determination of cases (c) and (d) in Fig. 12. It is too large for the

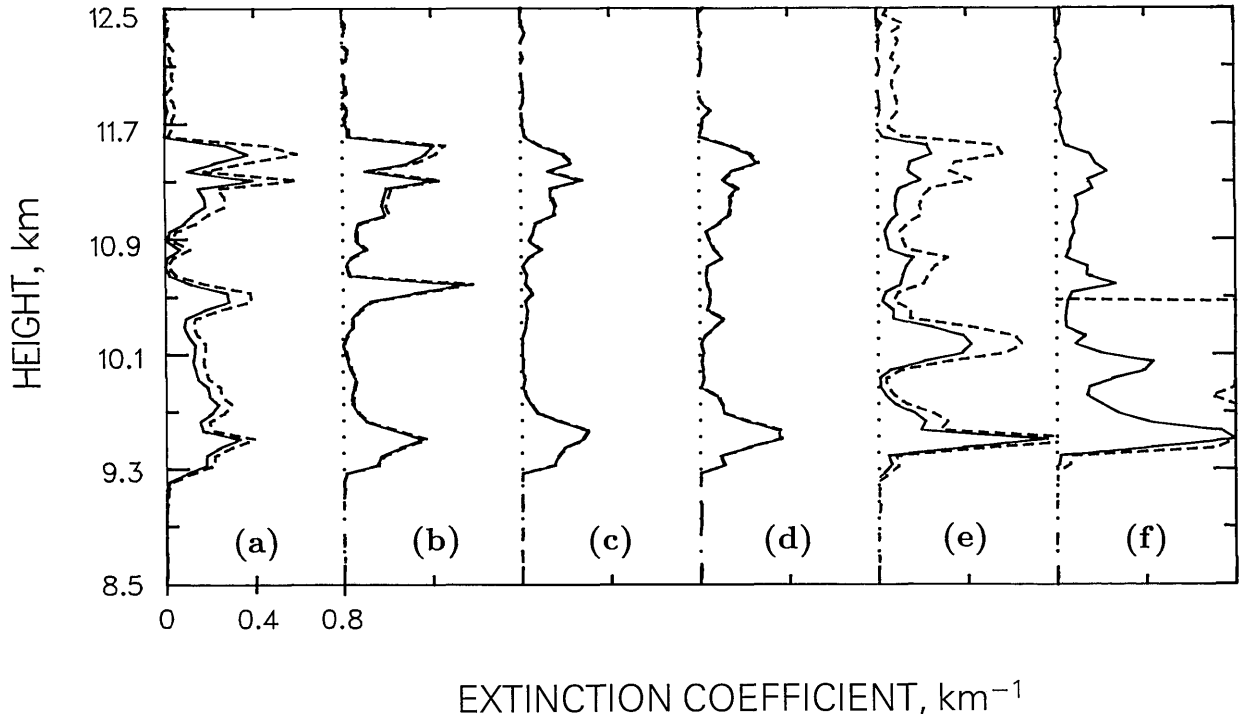

Fig. 12. Bernoulli solutions applying forward (dashed curve) and backward (solid curve) integration. The lidar measurement was taken in a cirrostratus deck on 18 October 1989 between 1129 and 1144 lt. Approximately 6,300 laser shots are averaged for each profile sampled in 150 s. Spatial resolution is 60 m. A lidar ratio $S_{\lambda_0}^{aer} = 13$ sr is selected. This lidar ratio can be seen to be appropriate in cases (c) and (d) only.

other cases. Forward integration begins to become unstable in case (e), and is completely unstable in case (f). Optimum range-independent lidar ratios are 10, 11.5, 7, and 5 sr for cases (a), (b), (e), and (f), respectively. The mean cloud lidar ratio varies between ~5 and 15 sr within a few minutes.

Our experience shows that for cirrus clouds of low optical depth, below ~0.5, the optimum extinction-to-backscatter ratio is roughly one half of the lidar ratio for which the forward integration solution becomes unstable. This result, which only holds for optically thin cirrus, was also found in a previous study[37] in which the forward integration method alone was used to determine the optimum cloud lidar ratio. Such a low cirrus optical depth was given over the whole day on 18 October 1989. Figure 13 summarizes the results of the measurement taken on that day. The time series of the cloud lidar ratio is shown in Fig. 13(d). Most of the Bernoulli solutions of forward integration became unstable for lidar ratios between 15 and 20 sr.

Figure 13 illustrates the usefulness of the Klett method for cirrus studies. For 115 profiles of the elastic-backscatter signal the optimum height-averaged lidar ratio is determined and used for the calculation of the maximum backscatter coefficient and the cloud optical depth. The ozone optical depth for the region between the two boundary heights of 6 and 12 km is 0.07 according to the standard model. Considering again an ozone uncertainty of ±100%, we find that the relative error of the optical depth and of the cloud lidar ratio is ~15%, 30%, and >50% for optical depths of 0.4, 0.2, and less than 0.1, respectively.

A closed cloud deck with rather smooth structures is observed for more than 5 h. Low wind speed (<15 m/s) and temperatures between −42°C (9 km) and −60°C (11.7 km) are measured in the cirrus layer. The cloud begins to form at the tropopause in the morning, one hour before the measurement was started, and disappears near sunset. The time series of the cloud top and base heights show a relatively large geometrical extension of the cloud that is persistent over several hours. While the cloud top is approximately constant, the base height varies considerably as a result of ice-crystal fall streaks crossing the RFOV.

Large maximum backscatter coefficients are observed between 1130 and 1230 lt, certainly caused by falling and, thus, horizontally oriented crystals. Together with the large backscatter peak at 1220 lt a very low lidar ratio of 2 sr is determined. As indicated in Fig. 13(a) (dashed curve), most of the maximum backscatter values, measured during the first half of the period shown, are found near the cloud base. Particle trails lead to a rapid increase of the cirrus geometric depth. In periods with low maximum backscatter coefficients, below 0.05 km^{-1}sr^{-1}, as is the case between 1440 and 1520 lt, the variability of the maximum backscatter height is largest. These variations appear to be caused by density fluctuations of the relatively homogeneously distributed particles. This interpretation is confirmed by the time series of backscatter height profiles. Sharp

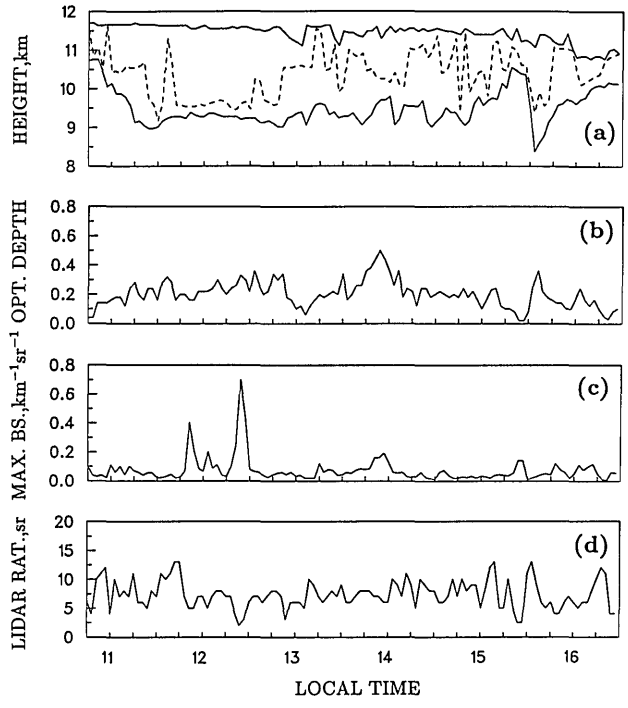

Fig. 13. Time series of cirrus top and base heights [(a), solid curve], the height at which the backscatter coefficient takes its maximum [dashed curve in (a)], cloud optical depth (b), maximum backscatter coefficient (c), and cloud lidar ratio (d) determined from the elastic backscatter signals by using the Klett method. The measurement was taken on 18 October between 1043 and 1628 lt. The temporal resolution is 150 s. The cloud lidar ratio is obtained by applying forward and backward integration. The maximum backscatter coefficient and the cloud optical depth are calculated with the shown cloud lidar ratio. RAT, ratio; BS, backscatter.

backscatter peaks, observed during the first half of the experiment, were seldom in the second half until 1520 lt, when the cloud began to dissolve.

The cloud optical depth is almost constant over the whole day. The strongest variability is observed in the middle and at the end of the cirrus life cycle. Small cloud lidar ratios are found that may indicate that the cirrus is composed mainly of small ice crystals.

6. Summary

For the first time to our knowledge, independent measurements of the backscatter and extinction profiles in high-level ice clouds have been made with a combined Raman elastic-backscatter lidar. The error analysis shows that realistic uncertainties in the atmospheric input parameters lead to relative systematic errors of the determined cirrus optical parameters of 10% to 20%. An additional error of more than 50% can be introduced if the optical properties vary strongly during the signal sampling and averaging period. Using the combined lidar technique, we can obtain height profiles of cirrus extinction, backscatter, and lidar ratio with a range resolution of 300 to 600 m, a time resolution of 5 to 20 min, and a statistical error of less than 20%.

Measurement examples obtained during ICE'89 indicate that the extinction and backscatter profiles of cirrus clouds can significantly differ from each other because of the dependence of the backscatter coefficient on shape, size, and orientation of the anisotropic ice particles, and they also indicate that the lidar ratio can thus vary strongly with time and height. For the first time, experimentally derived lidar ratios agree well with results of numerical calculations of ice-crystal scattering characteristics. Extinction-to-backscatter ratios between 5 and 15 sr have usually been measured during ICE'89, but variations between 2 and 20 sr have also been observed within one cloud.

The comparison of extinction profiles determined with the Raman and the Klett methods have shown that reliable extinction coefficients cannot be determined from elastic-backscatter signals alone. Because of the range variability of the lidar ratio the Bernoulli solution for $\alpha_{\lambda_0}^{aer}$ as well as the shape of the extinction profile can be incorrect. Only the backscatter coefficient profile is reliable. Conventional backscatter lidars can provide valuable information on the optical depth and the mean extinction-to-backscatter ratio of ice clouds if the forward and backward integration variants of the Klett procedure can be made to converge to the same extinction coefficient profile.

The authors acknowledge valuable discussions with W. Lahmann.

References

1. K. N. Liou, "Influence of cirrus clouds on weather and climate processes: a global perspective," Mon. Weather Rev. **114,** 1167–1199 (1986).
2. Issue on "First ISCCP regional experiment (FIRE)," Mon. Weather Rev. **118**(11) (1990).
3. D. Hennings, M. Quante, and R. Sefzig, "ICE—International Cirrus Experiment—1989 Field Phase Report" (Institut für Geophysik und Meteorologie, Universität zu Köln, Köln, Germany, 1990).
4. A. Ansmann, M. Riebesell, and C. Weitkamp, "Measurement of atmospheric aerosol extinction profiles with a Raman lidar," Opt. Lett. **15,** 746–748 (1990).
5. J. Cooney, J. Orr, and C. Tomasetti, "Measurements separating the gaseous and aerosol components of laser atmospheric backscatter," Nature (London) **224,** 1098–1099 (1969).
6. S. H. Melfi, "Remote measurements of the atmosphere using Raman scattering," Appl. Opt. **11,** 1605–1610 (1972).
7. F. G. Fernald, B. M. Herman, and J. A. Reagan, "Determination of aerosol height distributions by lidar," J. Appl. Meteorol. **11,** 482–489 (1972).
8. J. D. Klett, "Stable analytic inversion solution for processing lidar returns," Appl. Opt. **20,** 211–220 (1981).
9. F. G. Fernald, "Analysis of atmospheric lidar observations: some comments," Appl. Opt. **23,** 652–653 (1984).
10. Y. Sasano, E. V. Browell, and S. Ismail, "Error caused by using a constant extinction/backscatter ratio in the lidar solution," Appl. Opt. **24,** 3929–3932 (1985).
11. W. Hitschfeld and J. Bordan, "Errors inherent in the radar measurement of rainfall at attenuating wavelengths," J. Meteorol. **11,** 58–67 (1954).
12. S. T. Shipley, D. H. Tracy, E. W. Eloranta, J. T. Trauger, J. T. Sroga, F. L. Roesler, and J. A. Weinman, "High spectral

resolution lidar to measure optical scattering properties of atmospheric aerosols. 1: Theory and instrumentation," Appl. Opt. **22,** 3716–3724 (1983).
13. C. J. Grund and E. W. Eloranta, "The 27–28 October 1986 FIRE IFO cirrus case study: cloud optical properties determined by high spectral resolution lidar," Mon. Weather Rev. **118,** 2344–2355 (1990).
14. M. Riebesell, "Raman-Lidar zur Fernmessung von Wasserdampf-und Kohlendioxid-Höhenprofilen in der Troposphäre," Ph.D. dissertation, rep. GKSS 90/E/13 (1990) (Universität Hamburg, Hamburg, Germany, 1990).
15. U. Wandinger, "Entwicklung und Erprobung eines Filterpolychromators für ein Raman-Lidar," *Diplomarbeit,* rep. GKSS 90/E/48 1990 (Fachbereich Physik, Universität Hamburg, Hamburg, Germany, 1990).
16. D. R. Evans, *The Atomic Nucleus* (McGraw-Hill, New York, 1955) p. 785.
17. J. Bösenberg, A. Ansmann, S. Elouragini, P. H. Flamant, K. H. Klapheck, H. Linne, C. Loth, L. Menenger, W. Michaelis, P. Moerl, J. Pelon, W. Renger, M. Riebesell, C. Senff, P.-Y. Thro, U. Wandinger, and C. Weitkamp, "Measurements with lidar systems during the International Cirrus Experiment 1989," MPI rep. 60 (Max-Planck-Institut für Meteorologie, Hamburg, Germany, 1990).
18. D. A. Leonard and B. Caputo, "A single-ended atmospheric transmissometer," Opt. Eng. **13,** 10–14 (1974).
19. H. Hermann, L. Pantani, L. Stefanutti, and C. Werner, "Lidar measurements of the atmospheric visibility," Alta Freq. **43,** 732-468E–735-471E (1974).
20. L. V. Kravets, "On the restoration of profiles of some optical parameters of cirrus clouds using lidar techniques," Atmos. Opt. **2,** 146–148 (1989).
21. V. M. Mitev, I. V. Grigorov, V. B. Simeonov, I. F. Arshinov, and S. M. Bobrovnikov, "Raman lidar measurements of the atmospheric extinction coefficient profile," Bulg. J. Phys. **17,** 67–74 (1990).
22. H. C. van de Hulst, *Light Scattering by Small Particles* (Dover, New York, 1981), pp. 414–439.
23. L. T. Molina and M. J. Molina, "Absolute absorption cross sections of ozone in the 185- to 350-nm wavelength range," J. Geophys. Res. **91,** 14501–14508 (1986).
24. R. A. McClatchey, R. W. Fenn, J. E. A. Selby, F. E. Volz, and J. S. Garing, "Optical properties of the atmosphere," in *Handbook of Optics,* W. G. Driscoll, ed. (McGraw-Hill, New York, 1978), pp. 14-1–14-64.
25. P. B. Russel, T. J. Swissler, and M. P. McCormick, "Methodology for error analysis and simulation of lidar aerosol measurements," Appl. Opt. **18,** 3783–3797 (1979).
26. B. T. N. Evans, "Sensitivity of the backscatter/extinction ratio to changes in aerosol properties: implications for lidars," Appl. Opt. **27,** 3299–3305 (1988).
27. M. J. T. Milton and P. T. Woods, "Pulse averaging methods for a laser remote monitoring system using atmospheric backscatter," Appl. Opt. **26,** 2598–2603 (1987).
28. F. A. Theopold and J. Bösenberg, "Evaluation of DIAL measurements in presence of signal noise," in *Proceedings of the 14th International Laser Radar Conference* (Istituto di Ricerca sulle Onde Elettromagnetiche, Comitato Nazionale per le Scienze, Florence, Italy, 1988), pp. 209–211.
29. E. W. Eloranta and S. T. Shipley, "A solution for multiple scattering," in *Atmospheric Aerosols—Their Formation, Optical Properties, and Effects,* A. Deepak, ed. (Spectrum, Hampton, Va., 1982), pp. 227–239.
30. Y. Takano and K. N. Liou, "Solar radiative transfer in cirrus clouds—part I: single scattering and optical properties of hexagonal ice crystals," J. Atmos. Sci. **46,** 3–19 (1989).
31. K. E. Kunkel and J. A. Weinman, "Monte Carlo analysis of multiply scattered lidar returns," J. Atmos. Sci. **33,** 1772–1781 (1976).
32. K. Jayaweera and B. J. Mason, "The behaviour of free falling cylinders and cones in a viscous fluid," J. Fluid Mech. **22,** 709–720 (1965).
33. C. M. R. Platt, "Lidar backscatter from horizontal ice crystal plates," J. Appl. Meteorol, **17,** 482–488 (1978).
34. L. Thomas, J. C. Cartwright, and D. P. Wareing, "Lidar observations of the horizontal orientation of ice crystals in cirrus clouds," Tellus **42b,** 211–216 (1990).
35. J. D. Klett, "Lidar inversion with variable backscatter/extinction ratios," Appl. Opt. **24,** 1638–1643 (1985).
36. L. R. Bissonnette, "Sensitivity analysis of lidar inversion algorithms," Appl. Opt. **25,** 2122–2125 (1986).
37. C. M. R. Platt, "Remote sounding of high clouds: I. Calculation of visible and infrared optical properties from lidar and radiometer measurements," J. Appl. Meteorol. **18,** 1130–1143 (1979).
38. A. J. Heymsfield, "Cirrus uncinus generating cells and the evolution of cirriform clouds," J. Atmos. Sci. **32,** 799–808 (1975).
39. A. J. Heymsfield and C. M. R. Platt, "A parameterization of the particle size spectrum of ice clouds in terms of the ambient temperature and the ice water content," J. Atmos. Sci. **41,** 846–855 (1984).
40. Q. Cai and K. N. Liou, "Polarized light scattering by hexagonal ice crystals: theory," Appl. Opt. **21,** 3569–3580 (1982).
41. C. M. R. Platt, J. C. Scott, and A. C. Dilley, "Remote sensing of high clouds. Part VI: Optical properties of midlatitude and tropical cirrus," J. Atmos. Sci. **44,** 729–747 (1987).
42. C. M. R. Platt, J. D. Spinhirne, and W. D. Hart, "Optical and microphysical properties of a cold cirrus cloud: evidence for regions of small ice particles," J. Geophys. Res. **94,** 11151–11164 (1989).
43. R. G. Oraltay and J. Hallett, "Evaporation and melting of ice crystals: a laboratory study," Atmos. Res. **24,** 169–189 (1989).
44. R. G. Pinnick, S. G. Jennings, P. Chylek, C. Ham, and W. T. Grandy, "Backscatter and extinction in water clouds," J. Geophys. Res. **88,** 6787–6796 (1983).
45. R. H. Dubinsky, A. I. Carswell, and S. R. Pal, "Determination of cloud microphysical properties by laser backscattering and extinction measurements," Appl. Opt. **24,** 1614–1621 (1985).
46. K. Sassen and G. C. Dodd, "Homogeneous nucleation rate for highly supercooled cirrus cloud droplets," J. Atmos. Sci. **45,** 1357–1369 (1988).
47. A. Asano, "Transfer of solar radiation in optically anisotropic ice clouds," J. Meteorol. Soc. Jpn. **61,** 402–413 (1983).